Journal Pre-proof

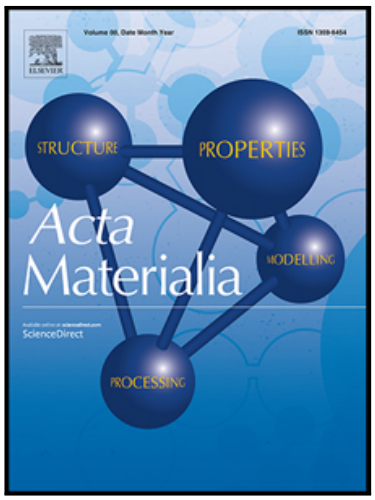


# Solid/liquid interface energy and its anisotropy of pure metals

Z. Fan , H. Men

PII: S1359-6454(26)00609-9
DOI: https://doi.org/10.1016/j.actamat.2026.122508
Reference: AM 122508

To appear in: *Acta Materialia*

Received date: 20 April 2026
Revised date: 19 June 2026
Accepted date: 27 June 2026

Please cite this article as: Z. Fan , H. Men , Solid/liquid interface energy and its anisotropy of pure metals, *Acta Materialia* (2026), doi: https://doi.org/10.1016/j.actamat.2026.122508

# Solid/liquid interface energy and its anisotropy of pure metals

Z. Fan* and H. Men
BCAST, Brunel University of London, Uxbridge, Middlesex, UB8 3PH, UK

*Corresponding author. Tel.: +44 1895 266406; Fax: +44 1895 269758; E-mail address: Zhongyun.Fan@brunel.ac.uk

**Abstract**

Solid/liquid (S/L) interface energy ($\gamma_{sl}$) and its anisotropy ($\varphi$) play a critical role in the understanding of nearly every single phenomenon that occurs during solidification of metals, such as nucleation, morphological instability and dendrite growth. However, due to difficulties associated with both experimental measurement and computer simulations, our current understanding of this topic is rather limited. In this work, a simple analytical model is developed to predict $\gamma_{sl}$ and $\varphi$ for pure metals. This model suggests that S/L interface energy originates from atomic ordering in the S/L interface templated by the solid. $\gamma_{sl}$ can be expressed as the sum of contributions from both atomic layering ($\gamma_z$) and the in-plane atomic ordering ($\gamma_{xy}$). Further analysis shows that $\gamma_{sl}$ for pure metals is determined by both heat of fusion per atom ($\Delta H_f^a$) and their crystal structures, while anisotropy depends only on crystal structure. The analytical model reveals that the physical origin of $\gamma_{sl}$ is atomic ordering in the S/L interface templated by the solid, while the physical origin of anisotropy is the difference in structural templating power between different crystal planes. It is demonstrated that the current analytical model is capable of predicting solid/liquid interface energy ($\gamma_{sl}$) and its anisotropy ($\varphi$) for any metallic element using parameters readily available in the literature.

**Keywords**: Solid/liquid interface energy; Anisotropy; Analytical modelling; Metals; Solidification.

## 1. Introduction

The solid/liquid (S/L) interface energy, $\gamma_{sl}$, is a key parameter in many fields of science and technology [1]. It plays a critical role in understanding nearly every single process during solidification of metals, such as crystal nucleation, morphological instability, dendrite formation and overall microstructural evolution [2]. Although the anisotropy in $\gamma_{sl}$ is usually small for metals with a diffuse S/L interface, it dictates the operating mechanisms of dendrite growth by selecting the preferred growth directions. However, our current understanding of interface energy and its anisotropy is limited due to difficulties associated with both experimental measurement and computer simulations [3].

Although a variety of other techniques have been investigated [4-6], experimental determination of $\gamma_{sl}$ has been following two main approaches: homogeneous nucleation [7] and grain boundary groove [8]. The homogeneous nucleation approach pioneered by Turnbull [7] is an indirect method based on the classical homogeneous nucleation theory, where he assumed that the nuclei had a spherical shape and the impurity that might lead to heterogeneous nucleation was eliminated. Turnbull's approach has so far provided most of the $\gamma_{sl}$ data for metals, nevertheless neither of the above assumptions is true in real experiments. For instance, the maximum undercooling achievable in metallic liquids has been found to be much larger than that reported by Turnbull, indicating that heterogeneous

nucleation was responsible for triggering solidification in Turnbull's experiments. The grain-boundary groove method developed by Hunt and co-workers [8] is a direct approach to obtain $\gamma_{sl}$ from the Read-Shockley formula [9]. This technique also suffers from drawbacks [10] and usually leads to an overestimate of $\gamma_{sl}$, with the uncertainty ranging from 15 to 30% [11]. Consequently, the currently available orientation-averaged $\gamma_{sl}$ data extracted from experiments are quite scattered. For instance, values of $\gamma_{sl}$ for pure aluminium determined experimentally by different investigators has a broad range: 93 mJ/m$^2$ [7], 97 mJ/m$^2$ [12], 102 mJ/m$^2$ [13], 108 mJ/m$^2$ [14], 122 mJ/m$^2$ [15], 157 mJ/m$^2$ [16], 158 mJ/m$^2$ [17]. Even worse, there is no experimental technique currently available to provide reliable data for anisotropy in $\gamma_{sl}$ for metals.

Model systems, such as colloidal suspensions and organic analogues, have been used to mitigate the difficulties associated with direct experimental investigation of metallic systems, taking advantage of the sluggish physical process and optical transparency provided by such systems [18]. Colloidal interactions can be experimentally tailored to display hard sphere (HS) behaviour and charged sphere (CS) exhibiting hardcore Yukawa repulsions or electrostatic attractions [19]. These systems have been employed to model many structural transitions known to metallic materials with body-centred cubic (BCC), face-centred cubic (FCC) and hexagonal close-packed (HCP) structures. For example, Palburg *et al*. [20] used a BCC crystalising colloidal suspension with charged spheres to derive $\gamma_{sl}$ and Turnbull's coefficient. They found that the average Turnbull's coefficient is 0.31±0.03 for BCC, which is consistent with other works in the literature [18,21-23]. More significantly, organic analogues have been used for experimental determinations of the anisotropy in $\gamma_{sl}$, based on the observed shape of either a small crystal surrounded by the melt or a melt inclusion within a crystal [24,25]. For instance, Glicksman and Singh [24] found that the BCC crystalising succinonitrile has a much weaker anisotropy in $\gamma_{sl}$ (0.5%) than that for the FCC crystalising pivalic acid (5%). However, transient effects and polydispersity of colloidal systems could cause significant discrepancy in the results of experiments even with the same system. A fundamental question is that to what extent such model systems can be directly compared to real systems of metals and alloys.

Molecular dynamics (MD) simulations have gained increasing importance in studying $\gamma_{sl}$ due to the advances in both computing capacity and simulation techniques in recent years [3]. According to its definition, $\gamma_{sl}$ is the excess energy of the coexisting system relative to the two bulk phases. The excess energy incurred in a diffuse S/L interface of pure metals is usually small compared with the total energy of the coexisting system, and thus it is particularly challenging to directly compute the S/L interface energy and its anisotropy with MD simulations [3]. To date, various techniques have been developed, such as the cleaving method [26-28], the capillary fluctuation method (CFM) [29-33], and the homogeneous nucleation (CN) method [34-37], as reviewed recently by Pasquale *et al*. [3] and Karma *et al*. [38]. The cleaving method is a direct assessment of $\gamma_{sl}$, but needs many trials to establish a stable interface in the calculation. Both CN and CFM are indirect methods. The CN method is straightforward to calculate $\gamma_{sl}$, nonetheless it cannot be used to determine the anisotropy. On the other hand, the CFM can extract $\gamma_{sl}$ and its anisotropy by analysing the equilibrium fluctuation spectrum of the S/L interface. However, the accuracy of $\gamma_{sl}$ calculated by all of these methods relies highly on the accuracy of the potentials used in the simulation and the details of the simulation techniques. An interesting fact is that interface energy data for the same system calculated from different potentials can be significantly different and this difference may be substantial even using the same potential but performed by different researchers [39]. Furthermore, the uncertainty in calculated interface energy by MD

simulation is around 5% [40], which is comparable with the anisotropy in $\gamma_{\mathrm{sl}}$ of metals, compromising the suitability of using MD simulation to assess anisotropy in $\gamma_{\mathrm{sl}}$.

To date, analytical modelling has been limited to the framework provided by Turnbull [7], who first proposed that $\gamma_{\mathrm{sl}}$ is linearly related to heat of fusion per atom ($\Delta H_f^a$) by fitting his experimental data. For instance, Skapski [12] introduced the contribution of surface tension of the liquid and entropy loss upon solidification to $\gamma_{\mathrm{sl}}$. Ewing [15] and Waseda et al., [13] considered the contribution of the reduced liquid entropy at the diffuse S/L interface due to atomic ordering. Miedema et al. [41,42] and Benedictus et al. [43] considered the contribution of heat of mixing and entropy of fusion for binary alloys. Gránásy et al. [44] considered the entropy loss of the liquid in contact with the crystal. Spaepen et al. [45,46] proposed a negentropic analytical model, positing that the origin of the S/L interface energy is mainly entropic in negative value. Despite such advances, an appropriate understanding of $\gamma_{\mathrm{sl}}$ and its anisotropy is still lacking [47].

In this work, we propose that a diffuse S/L interface is a consequence of atomic ordering templated in the interface by the solid. Based on this we have developed a simple analytical model to predict the S/L interface energy and its anisotropy. It is shown that the predicted interface energy and its anisotropy are largely in good agreement with both experimental results and MD simulations.

## 2. Atomic structure of the S/L interface

At its melting temperature ($T_{\mathrm{m}}$), the flat surfaces of a volume of solid (S) and a volume of liquid (L) of a pure metal are brought in contact with each other at the atomic level. Upon reaching equilibrium, a physical region of finite thickness is created between the solid and the liquid. This region has a distinctive atomic structure that is different from both the long-range order of the solid and the short-range order of the liquid. In contrast to the traditional Gibbs dividing S/L interface that has zero-thickness, this region of finite thickness is referred to as a diffuse S/L interface (Fig. 1a). Such a diffuse S/L interface can be viewed as a region between two imaginary planes: a solid plane beyond which there is no liquid atoms, and a liquid plane beyond which there is no atomic layering. Partial atomic ordering in the S/L interface can be characterised by two distinctive phenomena [48,49]:

- *Atomic layering*: which represents the atomic ordering along the direction parallel to the normal of the interface (the z direction in Fig. 1) and is quantitatively described by an exponential decay of peak atomic density, $\rho(\mathrm{z})$, as schematically illustrated in Fig. 1b.
- *In-plane atomic ordering*: which represents the atomic ordering in each atomic layer parallel to the interface (the xy plane) and is characterised by the in-plane order parameter (fraction of ordered atoms in each layer), $S(\mathrm{z})$, as schematically illustrated in Fig. 1c.

Recent MD simulations [50-52] reveal that atomic layering is independent of the atomic structure of the solid plane and thus isotropic, while in-plane atomic ordering is closely related to the atomic arrangement in the solid plane and thus is anisotropic by nature. From this point of view, atomic layering can be viewed as atomic ordering along the z direction templated by a structureless wall, while the in-plane atomic ordering in the xy plane is templated by the specific atomic arrangement in the solid plane [49].

At $T_{\mathrm{m}}$, the free energy of the solid per atom ($g_s^a$) equals the free energy of the liquid per atom ($g_l^a$). The interface energy, $\gamma_{\mathrm{sl}}$, is defined as the excess energy of the S/L interface per unit area, $\Delta G^{\mathrm{ex}}$, which is shown by the shaded area in Fig. 1d. Hence, one has

$$\gamma_{\mathrm{sl}} = \Delta G^{\mathrm{ex}}. \quad (1)$$

## 3. An analytical model for the diffuse S/L interface energy and its anisotropy

According to the previous analysis, the interface energy of a diffuse S/L interface ($\gamma_{\mathrm{sl}}$) is the excess energy of the interface per unit area, $\Delta G^{\mathrm{ex}}$, which consists of the contributions of both the atomic layering, $\gamma_{\mathrm{z}}$, and the in-plane atomic ordering, $\gamma_{\mathrm{xy}}$. Hence,

$$\gamma_{\mathrm{sl}} = \gamma_{\mathrm{z}} + \gamma_{\mathrm{xy}}. \quad (2)$$

$\gamma_{\mathrm{z}}$ and $\gamma_{\mathrm{xy}}$ will be quantified in the following sections.

### *3.1. Quantification of $\gamma_z$*

Although there have been many investigations of atomic layering in the liquid adjacent to a structureless wall (e.g. [53-55]), so far, no effort has been made to quantify the contribution of atomic layering to $\gamma_{\mathrm{sl}}$. MD simulation was used to quantify the contribution of atomic layering to the diffuse interface energy, $\gamma_{\mathrm{z}}$, using pure aluminium (Al) as a starting point. A simulation system of bulk liquid Al with 77760 atoms was equilibrated at varied temperatures ($T$) using LAMMPS [56] to create the reference states. The embedded-atom method (EAM) potential for Al, developed by Zope and Mishin [57], was employed to describe the interaction between Al atoms. A simulation system consisting of liquid Al (77760 atoms) between 2 structureless walls was then equilibrated at varied $T$, where the interaction between liquid atoms is described by the same EAM potential for Al [57] and the interaction between the wall and the liquid atoms is described by a Lennard-Jones potential:

$$E = 4\varepsilon\left[\left(\frac{\sigma_{LJ}}{z}\right)^{12} - \left(\frac{\sigma_{LJ}}{z}\right)^{6}\right], \quad (3)$$

where $z$ is the vertical distance between an atom and the structureless wall, $\varepsilon$ and $\sigma_{LJ}$ are parameters representing the bonding energy and the distance at which $\varepsilon$ is zero, respectively. Here, $\varepsilon$ and $\sigma_{LJ}$ were optimized to be 0.412 eV and 2.6485 Å, respectively, with a cutoff distance of 12 Å, by using the data of bulk liquid Al simulated with the EAM potential [57].

Fig. 2 shows the atomic number density profile, $\rho(\mathrm{z})$, of the liquid Al adjacent to a structureless wall as a function of distance ($z$) away from the wall equilibrated at $T$ = 900 K. The liquid exhibits profound atomic layering adjacent to the structureless wall, where the liquid atoms are only subject to the effect of the structureless wall. By comparing with the total energy of the bulk liquid Al (the reference system), the excess energy induced by the structureless wall is evaluated to be $\gamma_{\mathrm{z}} = 12$ mJ/m$^2$.

Intuitively, one would expect that $\gamma_{\mathrm{z}}$ should be related to both temperature and the heat of fusion per atom ($\Delta H_{\mathrm{f}}^{\mathrm{a}}$). To understand the temperature dependence of $\gamma_{\mathrm{z}}$, the simulation system of liquid Al in contact with a structureless wall was equilibrated to evaluate $\gamma_{\mathrm{z}}$ at varying undercoolings ($\Delta T$). The resultant $\gamma_{\mathrm{z}}$ values did not show any co-relationship to

temperature and subsequently such data were used to evaluate the standard deviation of $\gamma_z$, which is 6 mJ/m$^2$. Therefore, $\gamma_z$ is taken to be temperature independent and for Al

$$\gamma_z^{Al} = 12 \pm 6 \text{ mJ/m}^2. \quad (4)$$

As will be demonstrated later, S/L interface energy due to in-plane atomic ordering ($\gamma_{xy}$) is linearly related to $\Delta H_f^a/\pi r_a^2$, where $\Delta H_f^a$ is the heat of fusion per atom and $r_a$ is the effective atomic radius derived from the volume per atom (Table 1). It is assumed here that $\gamma_z$ is also linearly proportional to $\Delta H_f^a/\pi r_a^2$. Hence, for a given element one has:

$$\gamma_z = \mathcal{A}\frac{\Delta H_f^a}{\pi r_a^2}, \quad (5)$$

where $\mathcal{A}$ is a constant, $\mathcal{A} = \pi r_{Al}^2 \gamma_z^{Al}/\Delta H_f^{Al} = 0.056$, and $\Delta H_f^{Al} (= 1.74 \times 10^{-17}$ mJ/atom) is the heat of fusion of aluminium per atom and $r_{Al} (= 1.61$ Å) is the effective radius of an Al atom.

*3.2. Quantification of $\gamma_{xy}$*

As presented in Section 2, $\gamma_{xy}$ is a consequence of transforming some of the liquid atoms in the interface into solid ones through structural templating. At $T_m$, when a liquid atom with an effective atomic radius of $r_a$ in the interface is transformed into a solid atom through structural templating, the free energy change ($\Delta g_f^a$) is

$$\Delta g_f^a = \Delta H_f^a - T_m \Delta S_f^a = 0, \quad (6)$$

where $\Delta S_f^a$ is the entropy of fusion per atom. The resultant excess energy will be $\Delta H_f^a$ and the excess energy per unit area is $\Delta H_f^a/\pi r_a^2$. The total excess energy per unit area for a diffuse S/L interface due to structural templating will be:

$$\gamma_{xy} = f_s \frac{\Delta H_f^a}{\pi r_a^2}, \quad (7)$$

where $f_s$ is the average fraction of solid atoms in the atomic layers that contain solid atoms, i.e., $f_s$ is the ratio of the total number of solid atoms in the interface to the total number of atoms in the layers that contain solid atoms (excluding the layers that contain only liquid atoms).

For a given undercooling ($\Delta T = T_m - T$), when a liquid atom in the interface is transformed into a solid atom through structural templating, one has

$$\Delta g^a = \Delta H_f^a - T\Delta S_f^a \quad (8)$$

where $\Delta g^a = g_s^a - g_l^a$ is the free energy change per atom at temperature $T$, and $g_s^a$ and $g_l^a$ are the free energy per atom for the solid and liquid, respectively. As a good approximation under small undercoolings ($\Delta T$), both $\Delta H_f^a$ and $\Delta S_f^a$ can be treated as temperature independent. By combining Eqs (6) and (8) one has:

$$\Delta g^a = \Delta T \Delta S_f^a. \quad (9)$$

The excess energy of transforming a liquid atom into a solid atom at $T$ will be $\Delta H_{\mathrm{f}}^{\mathrm{a}} + \Delta g^{a}$. Following Eq. (7), $\gamma_{\mathrm{xy}}$ can be expressed as

$$\gamma_{\mathrm{xy}} = f_{\mathrm{s}} \frac{\Delta H_{\mathrm{f}}^{\mathrm{a}} + \Delta g^{a}}{\pi r_{\mathrm{a}}^{2}} = f_{\mathrm{s}} \frac{\Delta H_{\mathrm{f}}^{\mathrm{a}} + \Delta T \Delta S_{\mathrm{f}}^{\mathrm{a}}}{\pi r_{\mathrm{a}}^{2}}. \quad (10)$$

For simplicity, hereafter we will only discuss $\gamma_{\mathrm{sl}}$ at $T_{\mathrm{m}}$ unless otherwise specified.

By inserting Eqs. (5) and (7) into Eq. (2), one has the expression for a diffuse interface energy of a metallic element:

$$\gamma_{\mathrm{sl}} = (\mathcal{A} + f_{\mathrm{s}}) \frac{\Delta H_{\mathrm{f}}^{\mathrm{a}}}{\pi r_{\mathrm{a}}^{2}}. \quad (11)$$

The slope of a plot of $\gamma_{\mathrm{sl}}$ vs $\frac{\Delta H_{\mathrm{f}}^{\mathrm{a}}}{\pi r_{\mathrm{a}}^{2}}$ is $(\mathcal{A} + f_{\mathrm{s}})$, where $\mathcal{A}$ is independent of crystal orientation (i.e., isotropic) while $f_{\mathrm{s}}$ is dependent on crystal orientation (i.e., anisotropic). In addition, Eq. (11) implies that the contribution of atomic layering to $\gamma_{\mathrm{sl}}$ is quantitatively equivalent to an extra contribution by increasing $f_{\mathrm{s}}$ by 0.056 (i.e., $\mathcal{A}$). That means that the contribution from atomic layering is about 10% of $\gamma_{\mathrm{sl}}$, as indicated in Section 4.

Eq. (11) is universally applicable to all metallic elements/alloys for predicting their $\gamma_{\mathrm{sl}}$ with any crystal orientation as long as $f_{\mathrm{s}}$ is known. As demonstrated previously [58], $f_{\mathrm{s}}$ can be obtained from MD simulations using local bond-order analysis [59-62]. However, in the following section, $f_{\mathrm{s}}$ for pure metals will be derived analytically based on structural templating.

### *3.3. Quantification of $f_s$ for pure metals*

As described previously, solid atoms in the interface are outcomes of structural templating by a given solid plane, which is highly dependent on the crystal structure of the solid plane. *Structural templating* describes the phenomenon that a crystal plane provides potential energy minima where liquid atoms can be potentially transformed into solid atoms. Therefore, one would intuitively expect that $f_{\mathrm{s}}$ should be closely related to potential energy ($\mathcal{E}_{\mathrm{p}}$) of an adatom (denoted as A) located at the potential energy minima relative to its nearest neighbouring atoms in the solid plane (denoted as S), as shown in Fig. 3. An expression for $\mathcal{E}_{\mathrm{p}}$ will be derived here.

For a given atomic plane, an adatom (A) has $N_{\mathrm{a}}$ nearest neighbouring atoms (S) in the solid plane, i.e., the adatom has $N_{\mathrm{a}}$ A-S bonds. Each A-S bond has a bond energy of $\mathcal{E}_{\mathrm{c}}/N_{\mathrm{b}}$, where $\mathcal{E}_{\mathrm{c}}$ is the cohesive energy of a bulk solid atom and $N_{\mathrm{b}}$ is the number of coordinates in the bulk solid. Bond energy can be taken as the product of an attractive (or repulsive) force and the bond length ($\sigma$) between A and S atoms. The contribution of an S atom to structural templating depends on the projection of the attractive force along the plane normal scaled with $\cos(\theta) = d/\sigma$, where $\theta$ is the angle between the A-S bond and the solid plane normal and $d$ is the inter-plane spacing (Fig. 3). Hence, the contribution of an S atom to structural templating will be $(\mathcal{E}_{\mathrm{c}}/N_{\mathrm{b}})\cos(\theta) = (\mathcal{E}_{\mathrm{c}}/N_{\mathrm{b}})(d/\sigma)$. The potential energy ($\mathcal{E}_{\mathrm{p}}$) of an adatom will be the total contribution to structural templating from all the S atoms, i.e.,

$$\mathcal{E}_{\mathrm{p}} = \mathcal{E}_{\mathrm{c}} \frac{N_{\mathrm{a}}}{N_{\mathrm{b}}} \frac{d}{\sigma}. \tag{12}$$

Here we define the templating power ($P_{\mathrm{t}}$) of a solid plane as $\mathcal{E}_{\mathrm{p}}/\mathcal{E}_{\mathrm{c}}$, thus one has:

$$P_{\mathrm{t}} = \frac{\mathcal{E}_{\mathrm{p}}}{\mathcal{E}_{\mathrm{c}}} = \frac{N_{\mathrm{a}}}{N_{\mathrm{b}}} \frac{d}{\sigma}. \tag{13}$$

It is clear that $P_{\mathrm{t}}$ is a fraction that varies between 0 and 1; $P_{\mathrm{t}} = 1$ when the adatom is a solid atom and $P_{\mathrm{t}} = 0$ when the adatom is a liquid atom. Eq. (13) suggests that structural templating is a geometrical phenomenon and that $P_{\mathrm{t}}$ is closely related to the crystal structure but is independent of the chemical nature of the element (i.e., $\mathcal{E}_{\mathrm{c}}$). Table 1 lists $\sigma$, $d$, $N_{\mathrm{a}}$, $N_{\mathrm{b}}$, $P_{\mathrm{t}}$ and $r_{\mathrm{a}}$ for the low-index planes of FCC, BCC and HCP crystals.

It is assumed here that the solid fraction in a S/L interface, $f_{\mathrm{s}}$, is linearly proportional to $P_{\mathrm{t}}$. From the previous discussion, it is also expected that $f_{\mathrm{s}} \to 0$ when $P_{\mathrm{t}} \to 0$. Hence, one has:

$$f_{\mathrm{s}} = \mathcal{B} P_{\mathrm{t}} = \mathcal{B} \frac{N_{\mathrm{a}}}{N_{\mathrm{b}}} \frac{d}{\sigma}, \tag{14}$$

where the constant, $\mathcal{B}$, is the slope of the $f_{\mathrm{s}}$–$P_{\mathrm{t}}$ plot, which is dependent of neither the structural nor the chemical nature of the element if the element has metallic bonds.

It should be noted that Eq. (14) is applicable to low-index planes of high-symmetry crystal structures (such as FCC, BCC and HCP), where $d > r_{\mathrm{a}}$. However, for high-index planes of any crystal and many crystal planes of low-symmetry crystals (such as rhombohedral and orthorhombic), one has $d \leq r_{\mathrm{a}}$. In such cases, the nearest neighbouring atoms of an adatom could be located at several planes and the electron screening effect [63-65] must be taken into consideration. It is assumed here that the strength of electron screening is inversely proportional to the number of planes (i.e., 1/*n*, where *n*= 1, 2, 3, …) away from the adatom. For the i$^{\mathrm{th}}$ nearest neighbouring atom, $\sigma_{\mathrm{i}}$ is the distance between the adatom and the i$^{\mathrm{th}}$ nearest neighbouring atom, and $d_i$ is the distance between the adatom and the solid plane where the i$^{\mathrm{th}}$ nearest neighbouring atom is located. Thus, one has $d_i = nd$. The contribution of an individual neighbouring atom to the templating power must be calculated individually and hence Eq. (14) becomes:

$$f_{\mathrm{s}} = \mathcal{B} \frac{1}{N_{\mathrm{b}}} \sum_{i=1}^{N_{\mathrm{a}}} \left(\frac{d}{\sigma_{\mathrm{i}}}\right). \tag{15}$$

Inserting Eq. (14) into Eq. (11), one has the following equation for $\gamma_{\mathrm{sl}}$ at $T_{\mathrm{m}}$:

$$\gamma_{\mathrm{sl}} = (\mathcal{A} + \mathcal{B} P_{\mathrm{t}}) \frac{\Delta H_{\mathrm{f}}^{\mathrm{a}}}{\pi r_{\mathrm{a}}^2} = (\mathcal{A} + \mathcal{B} \frac{N_{\mathrm{a}}}{N_{\mathrm{b}}} \frac{d}{\sigma}) \frac{\Delta H_{\mathrm{f}}^{\mathrm{a}}}{\pi r_{\mathrm{a}}^2}. \tag{16}$$

For an arbitrary temperature ($T$) below $T_{\mathrm{m}}$, the excess energy for templating a solid atom will be $\Delta H_{\mathrm{f}}^{\mathrm{a}} + \Delta g^{a}$ instead of $\Delta H_{\mathrm{f}}^{\mathrm{a}}$ and $\gamma_{\mathrm{sl}}$ can be thus expressed as:

$$\gamma_{\mathrm{sl}} = (\mathcal{A} + f_{\mathrm{s}}) \frac{\Delta H_{\mathrm{f}}^{\mathrm{a}} + \Delta g^{a}}{\pi r_{\mathrm{a}}^2} = (\mathcal{A} + f_{\mathrm{s}}) \frac{\Delta H_{\mathrm{f}}^{\mathrm{a}} + \Delta T \Delta S_{\mathrm{f}}^{\mathrm{a}}}{\pi r_{\mathrm{a}}^2}. \tag{17}$$

Eq. (16) suggests that at $T_m$, $\gamma_{xy}$ $(= \gamma_{sl} - \gamma_z)$ is linearly proportional to $P_t \Delta H_f^a / \pi r_a^2$. Thus, parameter $\mathcal{B}$ can be determined by the slope of a plot of $\gamma_{xy}$ vs $P_t \Delta H_f^a / \pi r_a^2$. Experimental data from the literature [7,14,66-70] are used for $\gamma_{sl}$ and other parameters can also be obtained from the literature [71,72]. Such a plot is presented in Fig. 4 and a linear regression gives $\mathcal{B}$ = 2.24.

*3.4. Anisotropy in $\gamma_{sl}$*

Following the convention in the literature, anisotropy in $\gamma_{sl}$ ($\varphi$) between two S/L interfaces with $(h_1 k_1 l_1)$ and $(h_2 k_2 l_2)$ orientations can be defined by the following equation:

$$\varphi = \frac{\gamma(h_1 k_1 l_1) - \gamma(h_2 k_2 l_2)}{\gamma(h_1 k_1 l_1) + \gamma(h_2 k_2 l_2)}. \quad (18)$$

Eq. (18) is applicable to all metals and alloys. For low-index planes of high symmetry metals, by inserting Eq. (16) into Eq. (18), one has:

$$\varphi = \frac{P_t(h_1 k_1 l_1) - P_t(h_2 k_2 l_2)}{2\frac{\mathcal{A}}{\mathcal{B}} + P_t(h_1 k_1 l_1) + P_t(h_2 k_2 l_2)}. \quad (19)$$

Eq. (19) reveals that anisotropy in $\gamma_{sl}$ originates from the difference in templating power of crystal planes: the larger the difference in templating power, the stronger the anisotropy. Therefore, anisotropy is dependent only on crystal structure and is independent of atomic bond energy. The physical origin of anisotropy in $\gamma_{sl}$ can be investigated further by inserting Eq. (13) into Eq. (19):

$$\varphi = \frac{(N_a d)(h_1 k_1 l_1) - (N_a d)(h_2 k_2 l_2)}{2N_b \sigma\frac{\mathcal{A}}{\mathcal{B}} + (N_a d)(h_1 k_1 l_1) + (N_a d)(h_2 k_2 l_2)}. \quad (20)$$

Eq. (20) suggests that anisotropy between two low-index planes of high symmetry crystals is dictated by the difference in $N_a d$: the larger this difference is, the stronger the anisotropy. Eqs. (19) and (20) are only applicable to low-index planes of high symmetry crystals. For calculation of anisotropy of high-index planes of high symmetry crystals and any plane of low symmetry crystals Eq. (18) should be used. Table 2 gives a summary of anisotropy, $\varphi$, for FCC, BCC and HCP (Mg) and other crystal structures with low crystal symmetry.

## 4. Model prediction and validation

Eq. (14) was used to calculate $f_s$ at $T_m$ for pure metallic elements of high crystal symmetry (i.e., FCC, HCP and BCC) while Eq. (15) was used for elements of low crystal symmetry (e.g., rhombohedral and orthorhombic). The resulting $f_s$ data were used to calculate $\gamma_{sl}$ at $T_m$ using Eq. (11). The resultant $f_s$ and $\gamma_{sl}$ at $T_m$ for pure metallic elements are tabulated in Table 3 for FCC metals, Table 4 for HCP metals, Table 5 for BCC metals and Table 6 for other metals of low crystal symmetry.

To validate the model predictions, the calculated orientation-averaged $\gamma_{sl}$ at $T_m$ using Eq. (11) are compared in Fig. 5 with the corresponding $\gamma_{sl}$ derived from experiments using various techniques [7,14,66-70]. It is clear from Fig. 5 that the model predictions are in good agreement with experimental results for a broad range of metals available in the literature considering the difficulties associated with measuring S/L interface energy. Such good

agreement between model predictions and experimental data suggests that the present analytical model can be used to predict $\gamma_{\mathrm{sl}}$ at $T_{\mathrm{m}}$ for metallic elements with high confidence.

To understand the anisotropy of pure metals of different crystal structures, the $\gamma_{\mathrm{xy}}$ (= $\gamma_{\mathrm{sl}} - \gamma_{\mathrm{z}}$) data for S/L interfaces with {001}, {011} and {111} orientations in Tables 3-5 are plotted against $\frac{\Delta H_{\mathrm{f}}^{\mathrm{a}}}{\pi r_{\mathrm{a}}^2}$ for FCC metals (in blue), BCC metals (in red), HCP metals (in green) in Fig. 6. The numbers adjacent to the dashed lines represent $f_{\mathrm{s}}$, which are the slopes of the dashed lines. To contrast the anisotropy difference in different crystal structures, the areas covered by $\gamma_{\mathrm{xy}}$ of different crystals are marked in different colours: light blue for FCC (triangle OAB), light green for HCP (triangle OCD) and light red for BCC (triangle OEF). In addition, the $\gamma_{\mathrm{xy}}$ data for metals of low crystal symmetry are presented as a function of $\frac{\Delta H_{\mathrm{f}}^{\mathrm{a}}}{\pi r_{\mathrm{a}}^2}$ in Fig. 7, where crystal structures are marked with different colours, crystal orientations are marked by different symbols (circle for {001}/{10$\bar{1}$0}, square for {011}/{11$\bar{2}$0} and triangle for {111}/{0001}), and $f_{\mathrm{s}}$ are marked on each of the dashed lines. Table 2 and Figs. 6 and 7 suggest that: (1) FCC metals have the highest crystal symmetry but lowest anisotropy; (2) HCP metals are slightly less symmetrical and slightly more anisotropic than FCC metals; (3) BCC metals are less symmetrical and more anisotropic than FCC and HCP metals; and (4) metals with low crystal symmetry are generally more anisotropic than metals with high crystal symmetry. The general trend is that anisotropy increases with decreasing crystal symmetry.

## 5. Discussion

### *5.1. Turnbull's coefficient $C_T$*

As early as 1950, in his seminal work Turnbull [7] proposed an empirical equation to describe his experimental finding that $\gamma_{\mathrm{sl}}$ extracted from maximum undercooling experiments was linearly related to the heat of fusion per atom:

$$\gamma_0 \rho^{-2/3} = C_T \Delta H_{\mathrm{f}}^{\mathrm{a}}, \tag{21}$$

where $\gamma_0$ is the orientation-averaged S/L interface energy, $\rho$ is the atomic number density of the solid, $\rho^{-2/3}$ represents an effective measure of the interfacial area per atom by treating the atom as a cube, and $C_T$ is often referred to as Turnbull's coefficient in the literature. Turnbull's original experimental data suggest that $C_T$ is 0.45 for metals and 0.32 for semi-metals and non-metals. Over the last seven decades, there have been a number of assessments of $C_T$ for metals and colloidal systems. For example, Kelton [14] analysed the available experimental results for 28 metals and suggested that $C_T$= 0.43, followed by other determinations of $C_T$ = 0.55 for FCC metals simulated with the embedded atom method (EAM) potential [73] and $C_T$ = 0.31 for BCC crystalising colloidal charged sphere suspensions [20].

By comparing Eq. (21) with Eq. (11) one has:

$$C_{\mathrm{T}} = \frac{\rho^{-\frac{2}{3}}}{\pi r_{\mathrm{a}}^2}(\mathcal{A} + f_{\mathrm{s}}). \tag{22}$$

By noting that $\frac{1}{\rho} = \frac{4}{3}\pi r_a^3$ (i.e., the average volume of an atom) one has $\frac{\rho^{-2/3}}{\pi r_a^2}$ = 0.83, and hence

$$C_T = 0.83(\mathcal{A} + f_s). \quad (23)$$

It has long been speculated that $C_T$ is somehow associated with atomic arrangement at the S/L interface [73]. We have, for the first time, found that $C_T$ is closely associated with the fraction of solid atoms in the diffuse S/L interface, as suggested by Eq. (23). In Turnbull's formulation (Eq. (21)) an atom is approximated as a cube while in the Eq. (11) it is approximated as a sphere. Consequently, the effective projected area of an atom in Eq. (11) is scaled down by a factor of 0.83 from that in Eq. (21). It is argued here that a sphere approximation is more reasonable than a cube one since an atom is closer to a sphere than a cube.

Experimentally determined values of $\gamma_{sl}$ for FCC, BCC, HCP elements and other elements with low crystal symmetry are plotted against $\frac{\Delta H_f^a}{\pi r_a^2}$ in Fig. 8. The slopes obtained by linear regression are 0.57 for FCC, 0.58 for HCP, 0.55 for BCC and 0.51 for other metals. The corresponding Turnbull's coefficients are 0.47, 0.48, 0.46 and 0.42, respectively, for FCC, HCP, BCC elements and other elements with low crystal symmetry according to Eq. (23). The average $C_T$ over all metals is 0.46, which is very close to both Turnbull's (0.45) and Kelton's (0.43) assessments of $C_T$.

It is interesting to note that the short-dashed lines (marking different $f_s$) in Fig. 8 form a funnel with its vertex located at the origin of the plot. The opening of the funnel increases linearly with the increasing $\frac{\Delta H_f^a}{\pi r_a^2}$. This implies that if the experimentally determined orientation-averaged $\gamma_{sl}$ are plotted against $\frac{\Delta H_f^a}{\pi r_a^2}$, the scatter of the data should be more pronounced at higher $\frac{\Delta H_f^a}{\pi r_a^2}$. This is indeed the case, as shown by the funnel marked by the long-dashed lines in Fig. 8. Therefore, Turnbull's coefficient $C_T$ represents the average of atomic ordering in the S/L interface over all the crystal structures of concern. $C_T$ is associated with $f_s$ only when $\gamma_{sl}$ is plotted against $\frac{\Delta H_f^a}{\pi r_a^2}$ for elements with same crystal structure.

*5.2. The physical origin of $\gamma_{sl}$ and its anisotropy*

The current analytical model suggests that the physical origin of $\gamma_{sl}$ is *structural templating*. A crystal plane will template atomic layering in the liquid adjacent to it although this atomic layering is independent of the atomic arrangement in the solid plane. In addition to atomic layering, a crystal plane will template atomic ordering in each of the atomic layers by providing potential energy minima where liquid atoms can be potentially transformed into solid atoms. It is obvious that such in-plane atomic ordering is highly dependent on the atomic arrangement in the solid plane. The templating power ($P_t$) of a crystal plane (Eq. (13)) represents its ability to transform an adatom (i.e., a liquid atom siting in the energy minima) into a solid atom: when $P_t$ = 1 the adatom will become a solid atom, while when $P_t$ = 0 the adatom will remain as a liquid atom. It is important to realise that $P_t$ is only related to crystal structure and is independent of the chemical nature of the metal. The outcome of structural templating is solid atoms in the interface and the value of interface energy $\gamma_{sl}$ is determined by the fraction of solid atoms in the interface for a given metal.

According to Eq. (2), S/L interface energy ($\gamma_{\mathrm{sl}}$) originates from two sources: one is atomic layering ($\gamma_{\mathrm{z}}$) which is isotropic and the other is in-plane atomic ordering ($\gamma_{\mathrm{xy}}$) which is anisotropic. Therefore, the physical origin of anisotropy in $\gamma_{\mathrm{sl}}$ is the difference in structural templating power between individual crystal planes. Fig. 8 provides us with new insights, which will be discussed here.

Firstly, let us analyse the key physical parameters that affect $\gamma_{\mathrm{sl}}$. According to Eq. (11), $\gamma_{\mathrm{sl}}$ is determined by two parameters: (1) $f_{\mathrm{s}}$, which reflects the difference in templating power of different crystal orientations; and (2) $\frac{\Delta H_{\mathrm{f}}^{\mathrm{a}}}{\pi r_{\mathrm{a}}^2}$, which represents the latent heat released per atom or equivalently the entropy loss per atom upon solidification ($\Delta S_{\mathrm{f}}^{\mathrm{a}}$, since at $T_{\mathrm{m}}$ $\Delta H_{\mathrm{f}}^{\mathrm{a}} = T_{\mathrm{m}}\Delta S_{\mathrm{f}}^{\mathrm{a}}$). For a given metal $\frac{\Delta H_{\mathrm{f}}^{\mathrm{a}}}{\pi r_{\mathrm{a}}^2}$ is a constant and anisotropy is hence determined by the difference in templating power of different crystal planes, as described by Eq. (19) or Eq. (20). This scenario is relevant to morphological instability and dendrite growth, where anisotropy is crucial but the absolute difference in $\gamma_{\mathrm{sl}}$ is not important. However, for different metals with the same crystal structure ($f_{\mathrm{s}}$ is fixed), while the anisotropy parameter ($\varphi$) remains constant the absolute difference in $\gamma_{\mathrm{sl}}$ between two different crystal planes is linearly proportional to $\frac{\Delta H_{\mathrm{f}}^{\mathrm{a}}}{\pi r_{\mathrm{a}}^2}$. In such cases, $\frac{\Delta H_{\mathrm{f}}^{\mathrm{a}}}{\pi r_{\mathrm{a}}^2}$ is like a magnifier, and the larger the $\frac{\Delta H_{\mathrm{f}}^{\mathrm{a}}}{\pi r_{\mathrm{a}}^2}$ is, the stronger the anisotropy is. The latter scenario is very relevant to phenomena like dendrite orientation transition (DOT) [74,75], where the absolute difference in $\gamma_{\mathrm{sl}}$ ($\Delta\gamma_{\mathrm{sl}}$) rather than the relative difference ($\varphi$) is relevant. This implies that metals/alloys that have a smaller $\frac{\Delta H_{\mathrm{f}}^{\mathrm{a}}}{\pi r_{\mathrm{a}}^2}$ have more natural tendency to DOT than those with higher $\frac{\Delta H_{\mathrm{f}}^{\mathrm{a}}}{\pi r_{\mathrm{a}}^2}$.

Secondly, crystals of higher crystal symmetry have weaker anisotropy and *vice versa*. FCC and HCP ($c/a \approx 1.633$) crystals have the highest crystal symmetry and the highest atomic packing density (72% for FCC and close to 72% for HCP). Fig. 6 suggests that such crystals have the lowest anisotropy, as indicated by the light blue triangle OAB for FCC and light green triangle OCD for HCP crystals. Here, HCP crystals showing slightly stronger anisotropy due to deviation of $c/a$ ratio from the ideal value (1.63). On the other hand, BCC crystals have a lower crystal symmetry and lower atomic packing density (68%). They exhibit much stronger anisotropy than both FCC and HCP crystals, as suggested by the larger area of the light red triangle OEF in Fig. 6. Furthermore, crystals of low crystal symmetry, such as rhombohedral and orthorhombic crystals, exhibit the strongest anisotropy (Fig. 7 and Table 2) compared with those of higher crystal symmetry (FCC, HCP) (Fig. 6).

Thirdly, crystal planes of different crystal structures can have the same or similar templating power and thus have the same or similar $f_{\mathrm{s}}$ although they may have completely different interface energy ($\gamma_{\mathrm{sl}}$) and strength of anisotropy ($\varphi$). For example, FCC{011}, FCC{111}, and HCP{0001} interfaces have $f_{\mathrm{s}} \approx 0.46$ (the slope of line OB in Fig. 6), and FCC{001}, and BCC{001} interfaces have $f_{\mathrm{s}} \approx 0.53$ (the slope of line OA in Fig. 6). This implies that FCC{011} and FCC{111} interfaces may have similar growth rate, which is consistent with the recent theoretical prediction by Chattopadhyay et al. [76], who found that the growth velocities ($V$) of pure FCC Ni have the following order: $V\{001\} > V\{011\} \cong V\{111\}$. Similarly, the current model predicts that for an HCP metal HCP$\{10\bar{1}0\}$ and HCP$\{11\bar{2}0\}$ interfaces have closely matching $\gamma_{\mathrm{sl}}$ and thus similar growth rates. This prediction is in good agreement with the recent theoretical work of Sanchez-Burgos et al. [77], who found that for

a hard sphere HCP phase the solid/melt interface energy is 0.60, 0.59 and 0.55 (in $k_BT/\sigma^2$) for HCP$\{11\bar{2}0\}$, HCP$\{10\bar{1}0\}$ and HCP(0001) interfaces, respectively. This is also consistent with the recent experimental finding that HCP Mg $\{10\bar{1}0\}$ and $\{11\bar{2}0\}$ dendrites interchange easily [78,79].

*5.3. Anisotropy in $\gamma_{sl}$ of BCC metals*

The current analytical model predicts that BCC metals have a stronger anisotropy in $\gamma_{\mathrm{sl}}$ than both FCC and HCP metals, as shown by the larger area of triangle OEF (BCC) than that of triangles OAB (FCC) and OCD (HCP) in Fig. 6. Although there is currently no direct experimental anisotropy data for metals available to validate this prediction, it strongly supported by the experimentally derived orientation-averaged $\gamma_{\mathrm{sl}}$ data. The Turnbull's plot in Fig. 8 suggests that BCC metals have a comparable $C_{\mathrm{T}}$ (0.46) with that for FCC (0.47) and HCP (0.48) metals. The overall $C_{\mathrm{T}}$ for all the metals is 0.46, which is very close to Turnbull's original $C_{\mathrm{T}}$ (0.45). In addition, it is usually expected that closely packed crystals have higher crystal symmetry and hence weaker anisotropy. Therefore, one would intuitively expect that BCC metals would have stronger anisotropy than that of FCC metals.

However, the current model's prediction that BCC metals are more anisotropic than FCC metals is contradictory to the MD simulation results of Hoyt and coworkers [80]. These researchers used EAM potentials and the capillary fluctuation method (CFM) [29] to calculate $\gamma_{\mathrm{sl}}$ and its anisotropy for a number of BCC and FCC metals. They found that the resultant Turnbull's coefficient for BCC metals (0.29) was much lower than that for FCC metals (0.55), which is inconsistent with experimental results that $C_{\mathrm{T}} = 0.55$ [7]. They also found that BCC metals have weaker anisotropy compared with that of FCC metals, with the {001}/{011} anisotropy being 1–2.5% for FCC metals and 0.4–1.0% for BCC metals. Obviously, this contradiction warrants further investigation. Here we offer some discussion on the MD methodology. CFM monitors the fluctuations in the position of a wavy solid/liquid interface over the course of the MD simulation. Through calculations of interface stiffness, $\gamma_{\mathrm{sl}}$ and its anisotropy can be evaluated. Here we argue that it is the wavy S/L interface that causes the disappearance of the orientation-dependence of $\gamma_{\mathrm{sl}}$. A general understanding is that a wavy crystal/liquid interface consists of many low-index crystal facets with {001}, {011} and {111} orientations, which is similar to the case for high-index crystal surfaces [81]. Once stabilised (metastable) the proportions of such facets will be independent of crystal orientation of the solid. This means that the calculated $\gamma_{\mathrm{sl}}$ will be independent of starting crystal orientation and that the numerical values for $\gamma_{\mathrm{sl}}$ will be within the uncertainty of MD simulation, which is around 5%.

In addition, the current model's prediction that BCC metals are more anisotropic than FCC metals is also contradictory to the experimentally determined Turnbull's coefficient for BCC crystalising organic analogues and colloidal suspensions. Palburg et al. [20] found that $C_{\mathrm{T}} = 0.31$ for a BCC crystalising charged sphere suspension while Glicksman and Singh [24] found that the BCC crystalising succinonitrile has a much weaker anisotropy in $\gamma_{\mathrm{sl}}$ (0.5%) than that for the FCC crystalising pivalic acid (5%). It is interesting to note that predicted $f_{\mathrm{s}}$ for the BCC {111} interface is 0.35 (Fig. 6), which converts to $C_{\mathrm{T}} = 0.29$. It is difficult to know whether this has any physical truth in it considering that the BCC{111} interface has

the lowest $\gamma_{sl}$ or whether this might be just a coincidence. Nevertheless, this warrants further investigation.

Furthermore, there are currently no experimentally determined anisotropy data for metals and alloys available in the literature. The anisotropy data predicted by the current analytical model should be used with caution before validation by reliable experimental data.

## 6. Summary

A simple analytical model has been developed to predict the diffuse solid/liquid interface energy and its anisotropy for pure metals. This model suggests that a diffuse S/L interface is a consequence of atomic ordering in the adjacent liquid induced by a crystal plane through structural templating. Such atomic ordering in the interface can be described by atomic layering that is isotropic and in-plane atomic ordering in each layer that is strongly dependent on the crystal structure and thus anisotropic. Interface energy ($\gamma_{sl}$) can be expressed as the sum of contributions from both atomic layering ($\gamma_z$) and in-plane atomic ordering ($\gamma_{xy}$). The resultant equation reveals that $\gamma_{sl}$ is determined by two key parameters: one is the fraction of solid atoms in the interface ($f_s$) that is the consequence of structural templating, and the other one is the heat of fusion per atom ($\Delta H_f^a$) that reflects the chemical nature of the element. This analytical model reveals that anisotropy in $\gamma_{sl}$ originates from the difference in structural templating power ($P_t$) by different crystal planes. Therefore, anisotropy in $\gamma_{sl}$ depends strongly on crystal symmetry but not on chemical nature of the elements; the higher the crystal symmetry is, the weaker the anisotropy is. Among all metals, FCC metals have the weakest anisotropy; HCP metals have a slightly stronger anisotropy than FCC metals; BCC metals have stronger anisotropy than that of FCC and HCP metals; and metals with low crystal symmetry have the strongest anisotropy.

**Data availability**

All relevant experimental and theoretical data within the article will be provided by the corresponding author on reasonable request.

**CRediT authorship contribution statement**

Z. Fan: Conceptualization, Formal analysis, Funding acquisition, Methodology, Validation, Writing – review & editing, Writing – original draft, Project administration. H. Men: Data curation, Formal analysis, Methodology, Validation, Visualization, Writing – review & editing, Writing – original draft.

**Declaration of competing interest**

The authors declare that they have no known competing financial interests or personal relationships that could have appeared to influence the work reported in this paper.

**Acknowledgements**

The EPSRC is gratefully acknowledged for providing financial support under Grant No. EP/N007638/1.

**References**:

[1] K. Charles, Introduction to Solid State Physics, eighth ed., John Wiley & Sons, Inc, USA, 2005, pp.50.

[2] W. Kurz, D.J. Fisher, M. Rappaz, Fundamentals of Solidification, fifth ed., Switzerland, Trans Tech Publications Ltd, 2023.
[3] N.D. Pasquale, J. Algaba, P.M. de Hijes, I. Sanchez-Burgos, A.R. Tejedor, S.R. Yeandel, F.J. Blas, R.L. Davidchack, J.R. Espinosa, C.L. Freeman, J.H. Harding, B.B. Laird, E. Sanz, C. Vega, L. Rovigatti, Solid−liquid interfacial free energy from computer simulations: Challenges and recent advances, Chem. Rev. 125 (2025) 5003−5053.
[4] S. Liu, R.E. Napolitano, R. Trivedi, Measurement of anisotropy of crystal-melt interfacial energy for a binary Al–Cu alloy, Acta Mater. 49 (2001) 4271–4276.
[5] D.Y. Kwok, A.W. Neumann, Contact angle measurement and contact angle interpretation, Adv. Colloid. Interface Sci. 81 (1999) 167-249.
[6] A. Calvimontes, The measurement of the surface energy of solids using a laboratory drop tower, npj Microgravity 3 (2017) 25.
[7] D. Turnbull, Formation of crystal nuclei in liquid metals, J. Appl. Phys. 21 (1950) 1022–1028.
[8] D.R.H. Jones, Review: The free energies of solid-liquid interfaces, J. Mater. Sci. 9 (1974) 1-17.
[9] W.T. Read, W. Shockley, Dislocation models of crystal grain boundaries, Phys. Rev. 78 (1950) 275–289.
[10] K.W. Bai, K. Wang, M. Sullivan, Y.-W. Zhang, Prediction of the solid-liquid interface energy of a multicomponent metallic alloy via a solid-liquid interface sublattice model, J. Alloys Compd. 819 (2020) 152992.
[11] A. Bulla, Measurement of the solid-liquid interface energy in ternary alloy, Ph.D Thesis, RWTH Aachen University, 2012, p.134.
[12] A.S. Skapski, A theory of surface tension of solids: Application to metals, Acta Metall. 4 (1956) 576–582.
[13] Y. Waseda, W.A. Miller, Calculation of the crystal-melt interfacial energy from experimental radial distribution function data, Trans JIM. 19 (1978) 546–552.
[14] K.F. Kelton, Crystal nucleation liquids glasses, Solid State Phys. Adv. Res. Appl. 45 (1991) 75-177.
[15] R.H. Ewing, The free energy of the crystal-melt interface from the radial distribution function-further calculations, J. Cryst. Growth 11 (1972) 221–224.
[16] D. Camel, N. Eustathopoulos, P. Desré, Chemical adsorption and temperature dependence of the solid–liquid interfacial tension of metallic binary alloys, Acta Metall. 28 (1980) 239–247.
[17] N. Eustathopoulos, L. Coudurier, J.C. Joud, P. Desré, Tension interfaciale solide-liquide des systémes Al-Sn, Al-In et Al-Sn-In, J. Cryst. Growth 33 (1976) 105.
[18] D.M. Herlach, I. Klassen, P. Wetteand, D. Holland-Moritz, Colloids as model systems for metals and alloys: A case study of crystallization, J. Phys.: Condens. Matter 22 (2010) 153101.
[19] A. Yethiraj, Tunable colloids: control of colloidal phase transitions with tunable interactions, Soft Matter 3 (2007) 1099-1115.
[20] T. Palberg, P. Wette, D.M. Herlach, Equilibrium interfacial free energies and Turnbull coefficient for bcc crystallizing colloidal charged sphere suspensions, arXiv: Soft Condensed Matter, 2014.
[21] P. Wette, H.J. Schöpe, T. Palberg, Crystallization in charged two-component suspensions, J. Chem. Phys. 122 (2005) 144901.
[22] M.O. Robbins, K. Kremer, G.S. Grest, Phase diagram and dynamics of Yukawa systems, J. Chem. Phys. 88 (1988) 3286.

[23] A. Engelbrecht, H.J. Schöpe, Drastic variation of the microstructure formation in a charged sphere colloidal model system by adding merely tiny amounts of larger particles, Cryst. Growth Des. 10 (2010) 2258- 2266.
[24] M.E. Glicksman, N.B. Singh, Effects of crystal-melt interfacial energy anisotropy on dendritic morphology and growth kinetics, J. Cryst. Growth 98 (1989) 277-284.
[25] M. Muschol, D. Liu, H.Z. Cummins, Surface-tension-anisotropy measurements of succinonitrile and pivalic acid: Comparison with microscopic solvability theory, Phys. Rev. A 46 (1992) 1038.
[26] J. Broughton, G. Gilmer, Molecular dynamics investigation of the crystal-fluid interface. VI. Excess surface free energies of crystal-liquid systems, J. Chem. Phys. 84 (1986) 5759.
[27] R.L. Davidchack, B.B. Laird, Direct calculation of the hard-sphere crystal/melt interfacial free energy, Phys. Rev. Lett. 85 (2000) 4751.
[28] R.L. Davidchack, B.B. Laird, Direct calculation of the crystal-melt interfacial free energies for continuous potentials: Application to the Lennard-Jones system, J. Chem. Phys. 118 (2003) 7651.
[29] J. Hoyt, M. Asta, A. Karma, Method for computing the anisotropy of the solid-liquid interfacial free energy, Phys. Rev. Lett. 86 (2001) 5530.
[30] D. Sun, M. Asta, J. Hoyt, Kinetic coefficient of Ni solid-liquid interfaces from molecular-dynamics simulations, Phys. Rev. B 69 (2004) 024108.
[31] D. Sun, M. Asta, J. Hoyt, Crystal-melt interfacial free energies and mobilities in fcc and bcc Fe, Phys. Rev. B 69 (2004) 174103.
[32] D. Sun, M. Mendelev, C. Becker, K. Kudin, T. Haxhimali, M. Asta, J. Hoyt, A. Karma, D. Srolovitz, Crystal-melt interfacial free energies in hcp metals: A molecular dynamics study of Mg, Phys. Rev. B 73 (2006) 024116.
[33] J. Hoyt, M. Asta, Atomistic computation of liquid diffusivity, solid-liquid interfacial free energy, and kinetic coefficient in Au and Ag, Phys. Rev. B 65 (2002) 214106.
[34] X.-M. Bai, M. Li, Calculation of solid-liquid interfacial free energy: A classical nucleation theory based approach, J. Chem. Phys. 124 (2006) 124707.
[35] Y. Shibuta, T. Suzuki, Melting and solidification point of fcc-metal nanoparticles with respect to particle size: A molecular dynamics study, Chem. Phys. Lett. 498 (2010) 323.
[36] Y. Watanabe, Y. Shibuta, T. Suzuki, A molecular dynamics study of thermodynamic and kinetic properties of solid–liquid interface for BCC iron, ISIJ Int. 50 (2010) 1158.
[37] Y. Shibuta, Y. Watanabe, T. Suzuki, Growth and melting of nanoparticles in liquid iron: A molecular dynamics study, Chem. Phys. Lett. 475 (2009) 264.
[38] A. Kumar, T. Ceme, G.G. Andersson, Interfacial excess, interfacial tension, interfacial entropy, and tools to measure thermodynamic quantity at the solid-liquid interface, in: K. Wandelt, G. Bussetti (eds.), Encyclopedia of Solid-Liquid Interfaces, first ed., Elsevier, 2024, pp. 255−267.
[39] R. Yan, S.D. Ma, W.Z. Sun, T. Jing, H.B. Dong, The solid–liquid interface free energy of Al: A comparison between molecular dynamics calculations and experimental measurements, Comput. Mater. Sci. 184 (2020) 109910.
[40] J.R. Morris, Complete mapping of the anisotropic free energy of the crystal-melt interface in Al, Phys. Rev. B 66 (2002) 144104.
[41] A.R. Miedema, F.J.A. den Broeder, On the interfacial energy in solid–liquid and solid–solid metal combinations, Z. Metallkd. 70 (1979) 14–20.
[42] F.R. de Boer, R. Boom, W.C.M. Mattens, A.R. Miedema, A.K. Niessen, Cohesion in Metals: Transition Metal Alloys, Elsevier North Holland, Amsterdam, 1988.

[43] R. Benedictus, A. Böttger, E.J. Mittemeijer, Thermodynamic model for solid-state amorphization in binary systems at interfaces and grain boundaries, Phys. Rev. B 54 (1996) 9109–9125.
[44] L. Gránásy, M. Tegze, A. Ludwig, Solid–liquid interfacial free energy, Mater. Sci. Eng. *A* 133 (1991) 577–580.
[45] F. Spaepen, A structural model for the solid-liquid interface in monatomic systems, Acta Metall. 23 (1975) 729-743.
[46] F. Spaepen, R.B. Meyer, The surface tension in a structural model for the solid liquid interface, Scr. Metall. 10 (1976) 257-263.
[47] S. Lippmann, I.-H. Jung, M. Paliwal, M. Rettenmayr, Modelling temperature and concentration dependent solid/liquid interfacial energies, Phil. Mag. 96 (2016) 1-14.
[48] W.D. Kaplan, Y. Kauffmann, Structural order in liquids induced by interfaces with crystals, Annu. Rev. Mater. Res. 36 (2006) 1–48.
[49] H. Men, C.M. Fang, Z. Fan, Prenucleation at the liquid/substrate interface: An overview, Metals, 12 (2022) 1704.
[50] A. Hashibon, J. Adler, M.W. Finnis, W.D. Kaplan, Ordering at solid-liquid interfaces between dissimilar materials, Interface Sci. 9 (2001) 175–181.
[51] J.P. Palafox-Hernandez, B.B. Laird, M. Asta, Atomistic characterization of the Cu–Pb solid–liquid interface, Acta Mater. 59 (2011) 3137–3144.
[52] H. Men, Z. Fan, Prenucleation induced by crystalline substrates, Metall. Mater. Trans. A 49 (2018) 2766-2777.
[53] F. F. Abraham, Y. Singh, The structure of a hard-sphere fluid in contact with a soft repulsive wall, J. Chem. Phys. 67 (1977) 2384-2385.
[54] B. B. Laird, R. L. Davidchack, Wall-induced prefreezing in hard spheres: A thermodynamic perspective, J. Phys. Chem. C 111 (2007) 15952-15956.
[55] R. Benjamin, J. Horbach, Lennard-Jones systems near solid walls: Computing interfacial free energies from molecular simulation methods, J. Chem. Phys. 139 (2013) 084705.
[56] S. Plimpton, Fast parallel algorithms for short-range molecular dynamics, J. Comput. Phys. 117 (1995) 1.
[57] R.R. Zope, Y. Mishin, Interatomic potentials for atomistic simulations of the Ti-Al system, Phys. Rev. B 68 (2003) 024102.
[58] Z. Fan, H. Men, Y. Wang, Z. Que, A new atomistic mechanism for heterogeneous nucleation in the systems with negative lattice misfit: Creating a 2D template for crystal growth. Metals 11 (2021) 478.
[59] P.J. Steinhardt, D.R. Nelson, M. Ronchetti, Bond-orientational order in liquids and glasses, Phys. Rev. B 28 (1983) 784-805.
[60] J. Baumgartner, A. Dey, P.H.H. Bomans, C.L. Coadou, P. Fratzl, N.A.J.M. Sommerdijk, D. Faivre, Nucleation and growth of magnetite from solution, Nat. Mater. 12 (2013) 310-314.
[61] P.R. Ten Wolde, M.J. Ruiz-Montero, D. Frenkel, Numerical evidence for bcc ordering at the surface of a critical fcc nucleus, Phys. Rev. Lett. 75 (1995) 2714-2717.
[62] S. Auer, D. Frenkel, Numerical prediction of absolute crystallization rates in hard-sphere colloids, J. Chem. Phys. 120 (2004) 3015-3029.
[63] R. A. Johnson, Empirical potentials and their use in the calculation of energies of point defects in metals, J. Phys. F: Met. Phys. 3 (1973) 295.
[64] Y. Wang, W.-D. Miao, L.-X. Zhai, An effective screened Coulomb interaction in a quasi-one-dimensional system, Phys. Lett. A 378 (2014) 442-445.
[65] M. H. Müser, S. V. Sukhomlinov, L. Pastewka, Interatomic potentials: achievements and challenges, Adv. Phys.: X, 7 (2023) 2093129.

[66] B. Vinet, L. Magnusson, H. Fredriksson, P.J. Desr´e, Correlations between surface and interface energies with respect to crystal nucleation, J. Colloid Interface Sci. 255 (2002) 363–374.
[67] G.W. Lee, S. Jeon, D.-H. Kang, Crystal−liquid interfacial free energy of supercooled liquid Fe using a containerless technique, Cryst. Growth Des. 13 (2013) 1786−1792.
[68] G.W. Leea, S. Jeona, C. Parka, D.-H. Kang, Crystal–liquid interfacial free energy and thermophysical properties of pure liquid Ti using electrostatic levitation: Hypercooling limit, specific heat, total hemispherical emissivity, density, and interfacial free energy, Chem. Thermodynamics 63 (2013) 1–6.
[69] Y.C. Cho, Y.-H. Lee, S. Ganorkar, G.W. Lee, Crystal-liquid interfacial free energy and thermophysical properties of refractory Mo, Nb and Ta pure metal elements, Curr. Appl. Phys. 80 (2025) 151–157.
[70] Y.Q. Wang, F. Zheng, X.X. Lu, Z.B. Sun, Heterogeneous nucleation and dendritic growth of niobium under containerless electrostatic levitation, Trans. Nonferrous Metals Soc. China 34 (2024) 1333−1346.
[71] H. Sawamura, The relation between the entropy of fusion or the heat of fusion of the metallic elements and their crystal structure, Trans. JIM, 13 (1972) 225-230.
[72] E. A. Brandes, G. B. Brook, eds., Smithells Metals Reference Book, seventh ed., Butterworth-Heinemann Linacre House, Jordan Hill, Oxford, 1992.
[73] J.J. Hoyt, M. Asta, D.Y. Sun, Molecular dynamics simulations of the crystal–melt interfacial free energy and mobility in Mo and V, Philos. Mag. 86 (2006) 3651.
[74] T. Haxhimali, A. Karma, F. Gonzales, M. Rappaz, Orientation selection in dendritic evolution, Nat. Mater. 5 (2006) 660-664. doi: 10.1038/nmat1693,
[75] L. Wang, J.J. Hoyt, N. Wang, N. Provatas, C.W. Sinclair, Controlling solid-liquid interfacial energy anisotropy through the isotropic liquid, Nat. Commun. 11 (2020) 724.
[76] C. Chattopadhyay, S. Sangal, K. Mondal, A relook at the preferred growth direction of the solid–liquid interface during solidification of pure metals, Acta Mater. 58 (2010) 5342–5353.
[77] I. Sanchez-Burgos, E. Sanz, C. Vega, J.R. Espinosa, Fcc vs. hcp competition in colloidal hard-sphere nucleation: on their relative stability, interfacial free energy and nucleation rate, Phys. Chem. Chem. Phys. 23 (2021) 19611−19626.
[78] M. Wang, Y. Xu, Q. Zheng, S. Wu, T. Jing, N. Chawla, Dendritic growth in Mg-based alloys: Phase-field simulations and experimental verification by X-ray synchrotron tomography, Metall. Mater. Trans. A 45 (2014) 2562–2574. https://doi.org/10.1007/s11661-014-2200-x.
[79] J. Du, Z. Guo, A. Zhang, M. Yang, M. Li, S. Xiong, Correlation between crystallographic anisotropy and dendritic orientation selection of binary magnesium alloys, Sci. Rep. 7 (2017) 13600. https://doi.org/10.1038/s41598-017-12814-5.
[80] J.J. Hoyt, M. Asta, T. Haxhimali, A. Karma, R.E. Napolitano, R.Trivedi, B.B. Laird, J.R. Morris, Crystal–melt interfaces and solidification morphologies in metals and alloys, MRS Bulletin 29 (2004) 935–939. https://doi.org/10.1557/mrs2004.263.
[81] H.W. Liu, N. Valanoor, K. Bogle, X. Cheng, An empirical method for surface energy anisotropy determination in high symmetry crystals, ACS Omega 10 (2025) 45278–45289.

Table 1 Summary of bond length ($\sigma$) between an adatom (A) and its nearest neighbouring atoms (S) in the solid plane of the interface, inter-plane spacing ($d$), number of the nearest neighbouring S atoms in the solid plane for the A atom ($N_a$), number of coordinates in the bulk solid ($N_b$), templating power ($P_t$) and effective atomic radius ($r_a$) of FCC, BCC and HCP (Mg as an example) crystal structures. *a* and/or *c* are the lattice parameters.

| Interface | | $\sigma$ | $d$ | $N_a$ | $N_b$ | $P_t$ | $r_a$ |
|---|---|---|---|---|---|---|---|
| FCC | $\{001\}$ | $a/\sqrt{2}$ | $a/2$ | 4 | 12 | 0.236 | $\left(\frac{3}{16\pi}\right)^{1/3} a$ |
| | $\{011\}$ | $a/\sqrt{2}$<br>$a/\sqrt{2}$ | $\sqrt{2}a/4$<br>$a/\sqrt{2}$ | 4<br>1 | 12 | 0.208 | |
| | $\{111\}$ | $a/\sqrt{2}$ | $a/\sqrt{3}$ | 3 | 12 | 0.204 | |
| BCC | $\{001\}$ | $\sqrt{3}a/2$<br>$a$ | $a/2$<br>$a$ | 4<br>1 | 14 | 0.236 | $\left(\frac{3}{8\pi}\right)^{1/3} a$ |
| | $\{011\}$ | $\sqrt{3}a/2$<br>$a$ | $a/\sqrt{2}$<br>$a/\sqrt{2}$ | 2<br>2 | 14 | 0.218 | |
| | $\{111\}$ | $\sqrt{3}a/2$<br>$a$<br>$\sqrt{3}a/2$ | $a/2\sqrt{3}$<br>$a/\sqrt{3}$<br>$\sqrt{3}a/2$ | 3<br>3<br>1 | 14 | 0.157 | |
| HCP (Mg) | $\{11\bar{2}0\}$ | $\sqrt{a^2/3+c^2/4}$<br>$a$<br>$a$ | $a/2$<br>$a/2$<br>$a$ | 2<br>2<br>1 | 12 | 0.250 | $\left(\frac{3^{3/2}a^2c}{16\pi}\right)^{1/3}$ |
| | $\{10\bar{1}0\}$ | $\sqrt{a^2/3+c^2/4}$<br>$a$ | $a/\sqrt{3}$<br>$\sqrt{3}a/2$ | 2<br>2 | 12 | 0.241 | |
| | $\{0001\}$ | $\sqrt{a^2/3+c^2/4}$ | $c/2$ | 3 | 12 | 0.204 | |

Table 2 Summary of anisotropy, $\varphi$, in S/L interface energy ($\gamma_{sl}$) of FCC, BCC, HCP (Mg), Hex (Se), Rhomb (Bi), Orth (Ga), FCDC (Ge) and BCT (In) crystal structures.

| Interface | $\varphi_{(001)\rightarrow(011)}$ | $\varphi_{(011)\rightarrow(111)}$ | $\varphi_{(001)\rightarrow(111)}$ |
|---|---|---|---|
| FCC | 0.056 | 0.009 | 0.065 |
| BCC | 0.038 | 0.142 | 0.178 |
| HCP (Mg) | $\varphi_{(11\bar{2}0)\rightarrow(10\bar{1}0)}$ | $\varphi_{(10\bar{1}0)\rightarrow(0001)}$ | $\varphi_{(11\bar{2}0)\rightarrow(0001)}$ |
| | 0.018 | 0.069 | 0.087 |
| Hex (Se) | $\varphi_{(0001)\rightarrow(11\bar{2}0)}$ | $\varphi_{(11\bar{2}0)\rightarrow(10\bar{1}0)}$ | $\varphi_{(0001)\rightarrow(10\bar{1}0)}$ |
| | 0.056 | 0.119 | 0.174 |
| Rhomb (Bi) | $\varphi_{(001)\rightarrow(111)}$ | $\varphi_{(111)\rightarrow(011)}$ | $\varphi_{(001)\rightarrow(011)}$ |
| | 0.089 | 0.039 | 0.128 |
| Orth (Ga) | $\varphi_{(001)\rightarrow(011)}$ | $\varphi_{(011)\rightarrow(111)}$ | $\varphi_{(001)\rightarrow(111)}$ |
| | 0.053 | 0.011 | 0.064 |
| FCDC (Ge) | $\varphi_{(001)\rightarrow(111)}$ | $\varphi_{(111)\rightarrow(011)}$ | $\varphi_{(001)\rightarrow(011)}$ |
| | 0.066 | 0.091 | 0.156 |
| BCT (In) | $\varphi_{(1\bar{1}1)\rightarrow(001)}$ | $\varphi_{(001)\rightarrow(011)}$ | $\varphi_{(111)\rightarrow(011)}$ |
| | 0.03 | 0.102 | 0.132 |

Table 3 Summary of melting point ($T_{\mathrm{m}}$), effective atomic radius ($r_{\mathrm{a}}$), heat of fusion per atom ($\Delta H_f^a$), solid fraction ($f_{\mathrm{s}}$), and S/L interface energy ($\gamma_{\mathrm{sl}}$) for elements with FCC crystal structures. $\gamma_0$ is orientation-averaged $\gamma_{\mathrm{sl}}$.

| Elements | $T_{\mathrm{m}}$ | $r_{\mathrm{a}}$ | $\Delta H_{\mathrm{f}}^{\mathrm{a}}$ | $f_{\mathrm{s}}$ | | | | $\gamma_{\mathrm{sl}}$, mJ/m$^2$ | | | |
|---|---|---|---|---|---|---|---|---|---|---|---|
| | K | Å | $10^{-17}$mJ/atom | Average | {001} | {011} | {111} | $\gamma_0$ | {001} | {011} | {111} |
| Ag | 1233.8 | 1.63 | 1.84 | 0.483 | 0.527 | 0.466 | 0.456 | 119.6 | 129.4 | 115.8 | 113.7 |
| Al | 933.1 | 1.61 | 1.74 | 0.483 | 0.527 | 0.466 | 0.456 | 115.1 | 124.4 | 111.4 | 109.4 |
| Au | 1336.0 | 1.62 | 2.12 | 0.483 | 0.527 | 0.466 | 0.456 | 139.2 | 150.5 | 134.7 | 132.3 |
| Ca | 1115.0 | 2.21 | 1.39 | 0.483 | 0.527 | 0.466 | 0.456 | 48.7 | 52.6 | 47.1 | 46.3 |
| Co | 1768.0 | 1.45 | 2.57 | 0.483 | 0.527 | 0.466 | 0.456 | 211.2 | 228.4 | 204.4 | 200.7 |
| Cu | 1357.8 | 1.44 | 2.16 | 0.483 | 0.527 | 0.466 | 0.456 | 179.4 | 194.1 | 173.7 | 170.6 |
| Ir | 2719.0 | 1.52 | 4.32 | 0.483 | 0.527 | 0.466 | 0.456 | 319.0 | 344.9 | 308.7 | 303.2 |
| Ni | 1728.0 | 1.40 | 2.85 | 0.483 | 0.527 | 0.466 | 0.456 | 248.5 | 268.8 | 240.6 | 236.2 |
| Pb | 600.6 | 1.95 | 0.80 | 0.483 | 0.527 | 0.466 | 0.456 | 36.0 | 38.9 | 34.8 | 34.2 |
| Pd | 1828.1 | 1.55 | 2.77 | 0.483 | 0.527 | 0.466 | 0.456 | 198.6 | 214.8 | 192.2 | 188.8 |
| Pt | 2041.4 | 1.56 | 3.27 | 0.483 | 0.527 | 0.466 | 0.456 | 231.4 | 250.3 | 224.0 | 220.0 |
| Rh | 2237.0 | 1.51 | 3.75 | 0.483 | 0.527 | 0.466 | 0.456 | 282.1 | 305.1 | 273.0 | 268.1 |
| Sr | 1043.0 | 2.40 | 1.39 | 0.483 | 0.527 | 0.466 | 0.456 | 41.7 | 45.1 | 40.4 | 39.6 |

Table 4 Summary of $T_{\mathrm{m}}$, effective atomic radius ($r_{\mathrm{a}}$), heat of fusion per atom ($\Delta H_f^a$), solid fraction ($f_{\mathrm{s}}$), and S/L interface energy ($\gamma_{\mathrm{sl}}$) for elements with HCP crystal structures. $\gamma_0$ is orientation-averaged $\gamma_{\mathrm{sl}}$.

| Elements | $T_{\mathrm{m}}$ | $r_{\mathrm{a}}$ | $\Delta H_{\mathrm{f}}^{\mathrm{a}}$ | $f_{\mathrm{s}}$ | | | | $\gamma_{\mathrm{sl}}$, mJ/m² | | | |
|---|---|---|---|---|---|---|---|---|---|---|---|
| | K | Å | $10^{-17}$mJ/atom | Average | $\{11\bar{2}0\}$ | $\{10\bar{1}0\}$ | $\{0001\}$ | $\gamma_0$ | $\{11\bar{2}0\}$ | $\{10\bar{1}0\}$ | $\{0001\}$ |
| Be | 1560.0 | 1.27 | 2.03 | 0.519 | 0.564 | 0.543 | 0.450 | 229.3 | 247.1 | 239.0 | 201.8 |
| Cd | 594.2 | 1.74 | 1.06 | 0.511 | 0.541 | 0.517 | 0.476 | 63.4 | 66.7 | 64.0 | 59.5 |
| Er | 1795.0 | 1.98 | 2.85 | 0.519 | 0.564 | 0.543 | 0.450 | 133.7 | 144.1 | 139.3 | 117.6 |
| Ho | 1747.0 | 1.98 | 2.85 | 0.519 | 0.564 | 0.543 | 0.450 | 132.8 | 143.1 | 138.4 | 116.9 |
| Lu | 1936.0 | 1.95 | 3.20 | 0.519 | 0.563 | 0.542 | 0.451 | 154.2 | 166.0 | 160.5 | 136.2 |
| Mg | 923.0 | 1.80 | 1.46 | 0.518 | 0.559 | 0.538 | 0.455 | 82.5 | 88.5 | 85.5 | 73.5 |
| Ru | 2607.0 | 1.50 | 4.27 | 0.519 | 0.563 | 0.542 | 0.451 | 346.0 | 372.4 | 360.1 | 305.4 |
| β-Sc | 1811.0 | 1.84 | 2.67 | 0.518 | 0.562 | 0.541 | 0.452 | 144.6 | 155.5 | 150.3 | 127.9 |
| Tc | 2430.0 | 1.53 | 3.82 | 0.518 | 0.561 | 0.540 | 0.454 | 297.7 | 319.9 | 309.1 | 264.2 |
| Tb | 1633.0 | 2.00 | 2.71 | 0.519 | 0.563 | 0.542 | 0.451 | 124.4 | 133.9 | 129.5 | 109.8 |
| Tm | 1818.0 | 1.97 | 3.06 | 0.519 | 0.564 | 0.543 | 0.450 | 144.6 | 155.8 | 150.7 | 127.3 |
| Y | 1803.0 | 2.02 | 1.90 | 0.519 | 0.563 | 0.543 | 0.450 | 85.1 | 91.7 | 88.7 | 74.9 |
| Zn | 692.7 | 1.55 | 1.21 | 0.512 | 0.543 | 0.519 | 0.474 | 90.5 | 95.4 | 91.6 | 84.5 |

Table 5 Summary of $T_{\mathrm{m}}$, effective atomic radius ($r_{\mathrm{a}}$), heat of fusion per atom ($\Delta H_f^a$), solid fraction ($f_{\mathrm{s}}$), and S/L interface energy ($\gamma_{\mathrm{sl}}$) for elements with BCC crystal structures. $\gamma_0$ is orientation-averaged $\gamma_{\mathrm{sl}}$.

| Elements | $T_{\mathrm{m}}$ | $r_{\mathrm{a}}$ | $\Delta H_{\mathrm{f}}^{\mathrm{a}}$ | $f_{\mathrm{s}}$ | | | | $\gamma_{\mathrm{sl}}$, mJ/m$^2$ | | | |
|---|---|---|---|---|---|---|---|---|---|---|---|
| | K | Å | $10^{-17}$mJ/atom | Average | {001} | {011} | {111} | $\gamma_0$ | {001} | {011} | {111} |
| Ba | 1002.0 | 2.51 | 1.27 | 0.455 | 0.528 | 0.486 | 0.351 | 32.9 | 37.6 | 34.9 | 26.2 |
| Cr | 2180.0 | 1.43 | 3.47 | 0.455 | 0.528 | 0.486 | 0.351 | 275.0 | 314.3 | 291.8 | 219.0 |
| Cs | 302.8 | 3.03 | 0.35 | 0.455 | 0.528 | 0.486 | 0.351 | 6.2 | 7.0 | 6.5 | 4.9 |
| Dy | 1682.0 | 1.92 | 2.85 | 0.455 | 0.528 | 0.486 | 0.351 | 125.7 | 143.6 | 133.3 | 100.1 |
| Eu | 1099.0 | 2.32 | 1.74 | 0.455 | 0.528 | 0.486 | 0.351 | 52.5 | 60.0 | 55.7 | 41.8 |
| δ-Fe | 1811.0 | 1.41 | 2.52 | 0.455 | 0.528 | 0.486 | 0.351 | 205.8 | 235.1 | 218.3 | 163.8 |
| β-Gd | 1585.0 | 1.99 | 2.57 | 0.455 | 0.528 | 0.486 | 0.351 | 106.1 | 121.3 | 112.6 | 84.5 |
| β-Hf | 2506.0 | 1.74 | 4.00 | 0.455 | 0.528 | 0.486 | 0.351 | 214.2 | 244.8 | 227.2 | 170.6 |
| K | 336.2 | 3.03 | 0.40 | 0.455 | 0.528 | 0.486 | 0.351 | 7.0 | 8.0 | 7.4 | 5.6 |
| Li | 453.7 | 1.74 | 0.49 | 0.455 | 0.528 | 0.486 | 0.351 | 24.3 | 29.9 | 27.7 | 20.8 |
| δ-Mn | 1519.0 | 1.41 | 2.44 | 0.455 | 0.528 | 0.486 | 0.351 | 213.1 | 243.7 | 226.1 | 169.3 |
| Mo | 2896.0 | 1.57 | 5.91 | 0.455 | 0.528 | 0.486 | 0.351 | 390.4 | 446.1 | 414.1 | 310.8 |
| Na | 370.9 | 2.12 | 0.44 | 0.455 | 0.528 | 0.486 | 0.351 | 15.8 | 18.1 | 16.8 | 12.6 |
| Nb | 2750.0 | 1.65 | 4.87 | 0.455 | 0.528 | 0.486 | 0.351 | 289.8 | 331.1 | 307.4 | 230.7 |
| Ta | 3290.0 | 1.66 | 4.10 | 0.455 | 0.528 | 0.486 | 0.351 | 243.2 | 277.9 | 258.0 | 193.7 |
| β-Th | 2023.0 | 2.03 | 3.13 | 0.455 | 0.528 | 0.486 | 0.351 | 123.5 | 141.1 | 131.0 | 98.3 |
| β-Ti | 1668.0 | 1.65 | 2.91 | 0.455 | 0.528 | 0.486 | 0.351 | 174.8 | 199.7 | 185.4 | 139.2 |
| β-Tl | 577.0 | 1.92 | 0.71 | 0.455 | 0.528 | 0.486 | 0.351 | 31.7 | 36.2 | 33.6 | 25.2 |
| V | 2183.0 | 1.52 | 2.78 | 0.455 | 0.528 | 0.486 | 0.351 | 197.1 | 225.2 | 209.1 | 156.9 |
| W | 3695.0 | 1.58 | 5.85 | 0.455 | 0.528 | 0.486 | 0.351 | 380.2 | 434.5 | 403.4 | 302.8 |
| γ-Yb | 1097.0 | 2.01 | 1.53 | 0.455 | 0.528 | 0.486 | 0.351 | 61.9 | 70.7 | 65.7 | 49.3 |
| β-Zr | 2125.0 | 1.80 | 3.20 | 0.455 | 0.528 | 0.486 | 0.351 | 161.9 | 185.0 | 171.8 | 128.9 |

Table 6 Summary of $T_{\mathrm{m}}$, effective atomic radius ($r_{\mathrm{a}}$), heat of fusion per atom ($\Delta H_f^a$), solid fraction ($f_{\mathrm{s}}$), and S/L interface energy ($\gamma_{\mathrm{sl}}$) for elements with low crystal symmetry. $\gamma_0$ is orientation-averaged $\gamma_{\mathrm{sl}}$.

| Elements | $T_{\mathrm{m}}$ K | $r_{\mathrm{a}}$ Å | $\Delta H_{\mathrm{f}}^{\mathrm{a}}$ $10^{-17}$mJ/atom | $f_{\mathrm{s}}$ | | | | $\gamma_{\mathrm{sl}}$ mJ/m$^2$ | | | |
|---|---|---|---|---|---|---|---|---|---|---|---|
| Hexagonal | | | | Average | {0001} | $\{11\bar{2}0\}$ | $\{10\bar{1}0\}$ | $\gamma_0$ | {0001} | $\{11\bar{2}0\}$ | $\{10\bar{1}0\}$ |
| Se | 494.0 | 1.92 | 1.04 | 0.669 | 0.781 | 0.692 | 0.533 | 65.2 | 75.3 | 67.3 | 53.0 |
| Te | 722.7 | 2.06 | 2.92 | 0.670 | 0.774 | 0.698 | 0.537 | 146.2 | 181.4 | 164.6 | 129.5 |
| Rhombohedral | | | | Average | {001} | {111} | {011} | $\gamma_0$ | {001} | {111} | {011} |
| Bi | 544.7 | 2.17 | 1.81 | 0.582 | 0.677 | 0.558 | 0.512 | 78.3 | 90.0 | 75.3 | 69.6 |
| Hg | 234.3 | 1.96 | 0.39 | 0.522 | 0.451 | 0.523 | 0.593 | 18.4 | 16.2 | 18.5 | 20.7 |
| Sb | 903.8 | 1.97 | 3.30 | 0.553 | 0.666 | 0.528 | 0.465 | 165.3 | 195.9 | 158.6 | 141.4 |
| Orthorhombic | | | | Average | {001} | {011} | {111} | $\gamma_0$ | {001} | {011} | {111} |
| Ga | 302.9 | 1.66 | 0.93 | 0.541 | 0.589 | 0.524 | 0.512 | 64.1 | 69.2 | 62.2 | 60.9 |
| Face-centered diamond cubic | | | | Average | {001} | {111} | {011} | $\gamma_0$ | {001} | {111} | {011} |
| Ge | 1211.4 | 1.77 | 6.11 | 0.553 | 0.645 | 0.559 | 0.456 | 378.3 | 435.4 | 381.6 | 318.0 |
| Si | 1687.0 | 1.70 | 8.41 | 0.553 | 0.645 | 0.559 | 0.456 | 568.0 | 653.5 | 573.1 | 477.4 |
| Body-centered tetragonal | | | | Average | {111} | {001} | {011} | $\gamma_0$ | {111} | {001} | {011} |
| In | 429.7 | 1.86 | 0.54 | 0.521 | 0.583 | 0.547 | 0.434 | 29.0 | 32.1 | 30.2 | 24.6 |
| β-Sn | 505.1 | 1.91 | 1.18 | 0.519 | 0.592 | 0.511 | 0.453 | 59.2 | 66.7 | 58.5 | 52.5 |

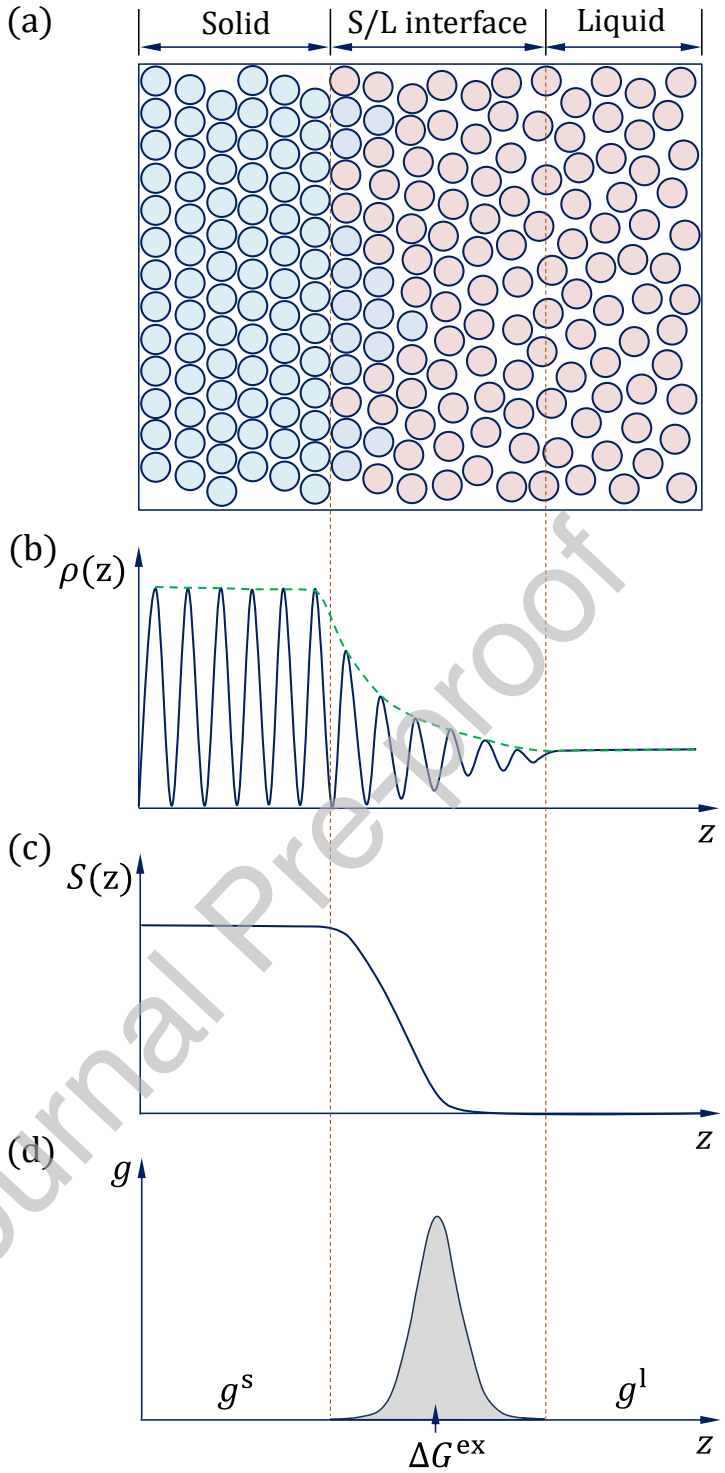


Fig. 1. Schematic illustration of the physical model for a diffuse solid/liquid (S/L) interface of a pure metal. The diffuse S/L interface (a) exhibits profound atomic ordering within 6 atomic layers. Such atomic ordering is manifested by (b) atomic layering with an exponential decay of peak atomic density ($\rho$(z)) and (c) in-plane atomic ordering quantified by the in-plane order parameter ($S$(z)), defined as the fraction of solid atoms in each layer. The S/L interface energy is attributed to the excess Gibbs free energy per unit area, $\Delta G^{ex}$, of the interface (d). The light blue and light red spheres in (a) represent solid and liquid atoms, respectively. $g^s$ and $g^l$ are the Gibbs free energy of bulk solid and liquid, respectively.

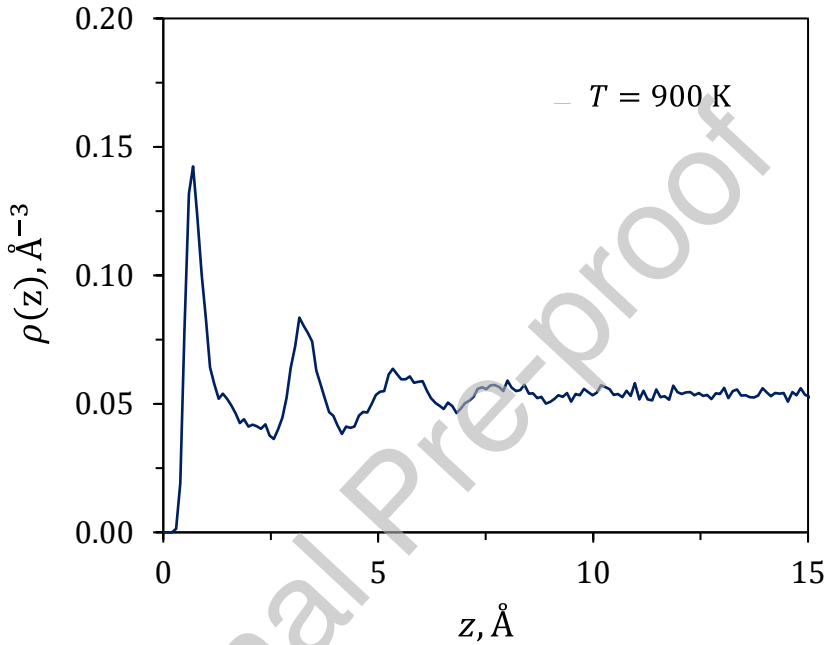


Fig. 2. Atomic density profile, $\rho(z)$, of the liquid Al adjacent to a structureless wall as a function of distance ($z$) from the wall equilibrated at $T$ = 900 K, showing a layered structure at the interface.

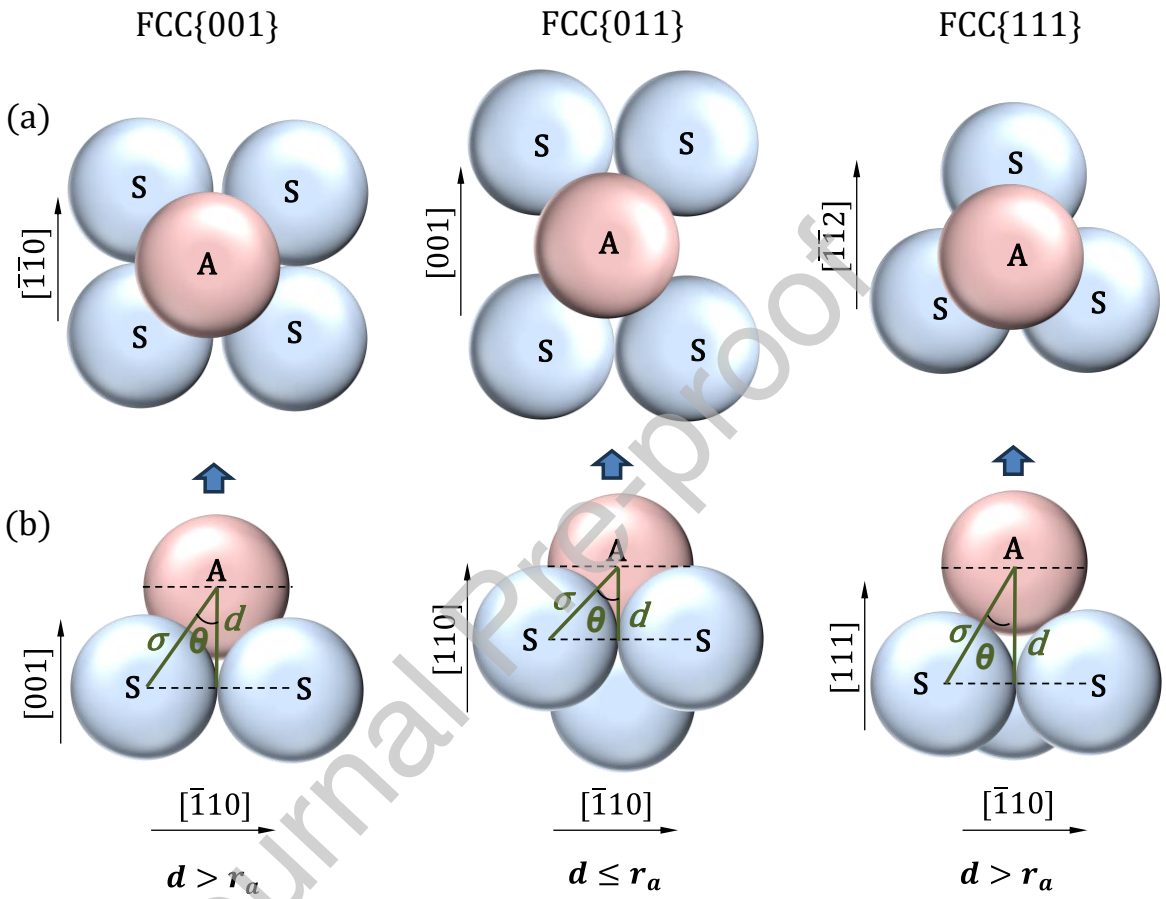


Fig. 3. Schematic illustration of the geometrical parameters that define the position of an adatom (A) relative to its nearest neighbouring atoms (S) located in a crystal plane of FCC structure with low-index orientations. (a) Top views and (b) side views. $r_a$ is the radius of the atoms.

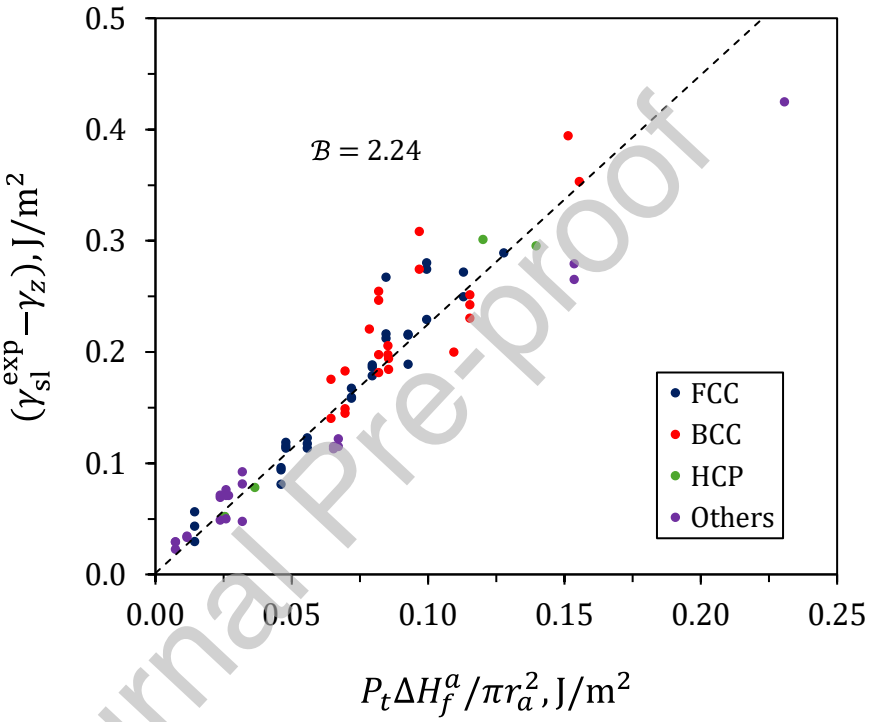


Fig. 4. $(\gamma_{sl}^{exp} - \gamma_z)$ as a function of $P_t \Delta H_f^a / \pi r_a^2$ for FCC, BCC, HCP elements and other elements with low crystal symmetry, where $\gamma_{sl}^{exp}$ is the experimental S/L interface energy taken from the literature [7,14,66-70]. Linear regression gives $\mathcal{B}$ = 2.24.

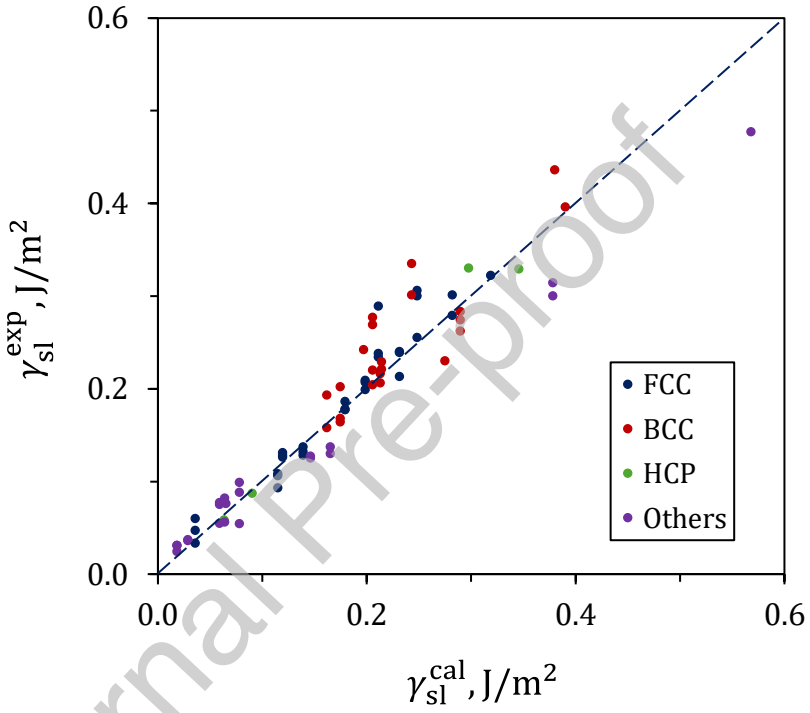


Fig. 5. Comparison of the calculated $\gamma_{sl}$ from the current analytical model with experimental values taken from literature [7,14,66-70].

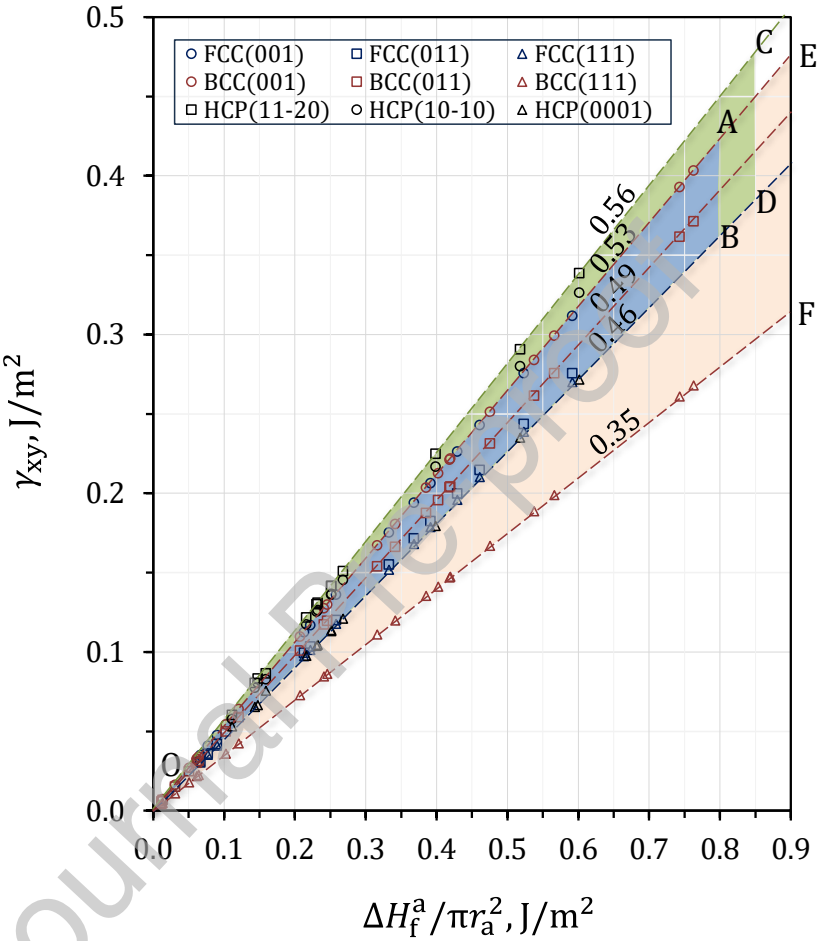


Fig. 6. The calculated $\gamma_{xy}$ as a function of $\Delta H_f^a/\pi r_a^2$ for FCC, BCC, HCP crystal structures with low index planes. The areas covered by $\gamma_{xy}$ of individual structures are coloured with light blue, green and red, respectively, for FCC (triangle OAB), HCP (triangle OCD) and BCC (triangle OEF). The numbers adjacent to the dashed lines represents $f_s$ of high and low boundaries of the coloured areas.

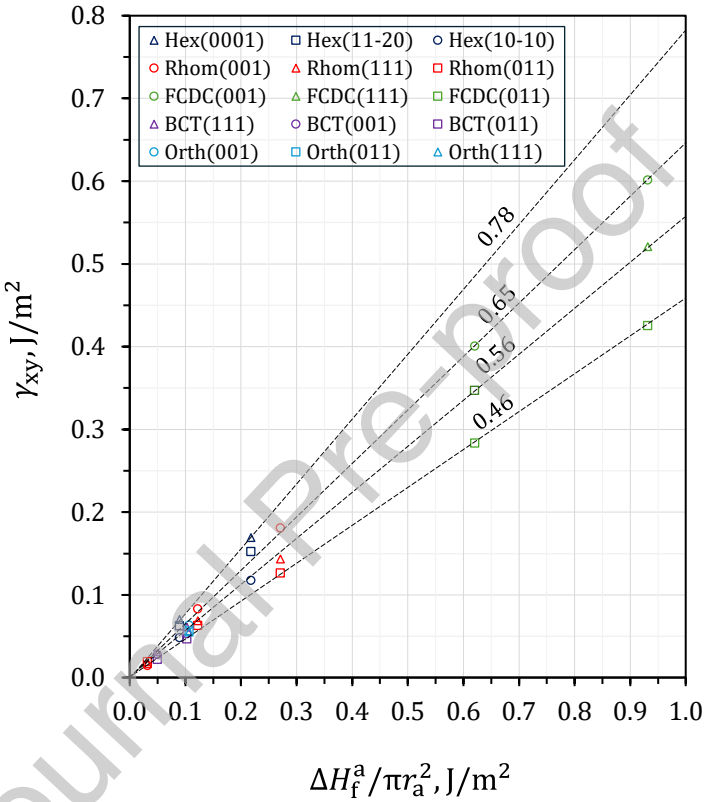


Fig. 7. Calculated $\gamma_{xy}$ as a function of $\Delta H_f^a/\pi r_a^2$ for elements with low crystal symmetry. The numbers adjacent to the dashed lines represent $f_s$, the slope of each dashed line.

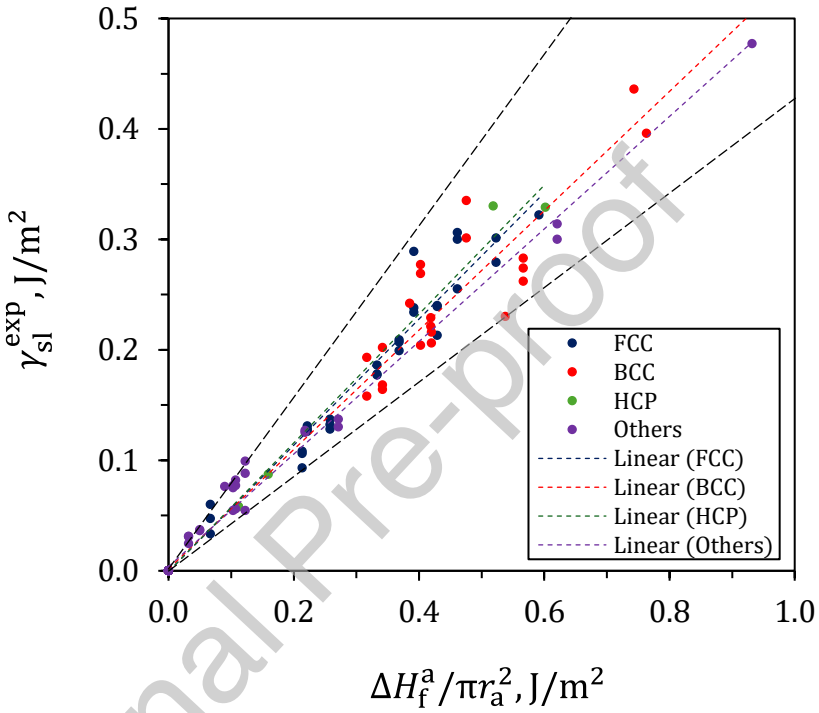


Fig. 8. Experimental values of $\gamma_{sl}$ plotted as a function of $\Delta H_f^a/\pi r_a^2$ for FCC, BCC, HCP elements and other elements with low crystal symmetry. The short-dashed lines represent the fitted slope of $\gamma_{sl}^{exp}$ against $\Delta H_f^a/\pi r_a^2$ for each crystal structure, where the slope is 0.57, 0.55, 0.58 and 0.51 respectively, for FCC, BCC, HCP elements and other elements with low symmetry. The average slope for all metals is 0.55. The long-dashed lines represent the envelope for the scattered data showing increasing data scatter with increasing $\Delta H_f^a/\pi r_a^2$.

Graphical abstract

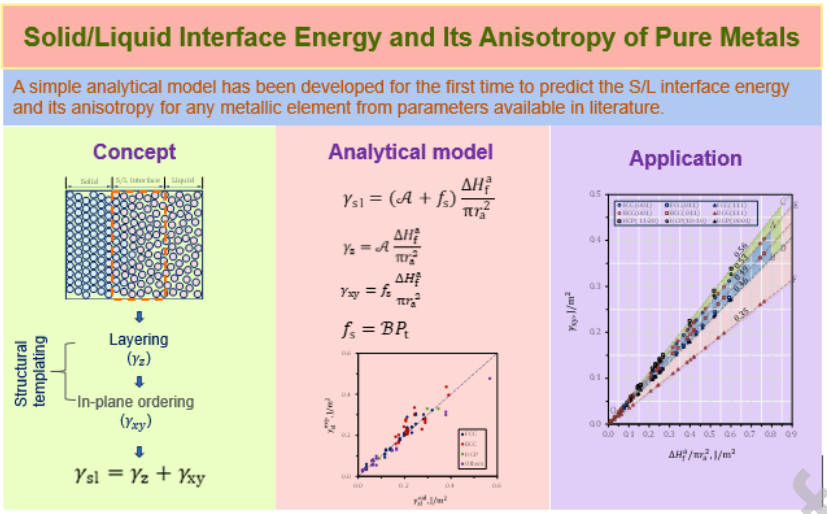


**Declaration of competing interest**

The authors declare that they have no known competing financial interests or personal relationships that could have appeared to influence the work reported in this paper.